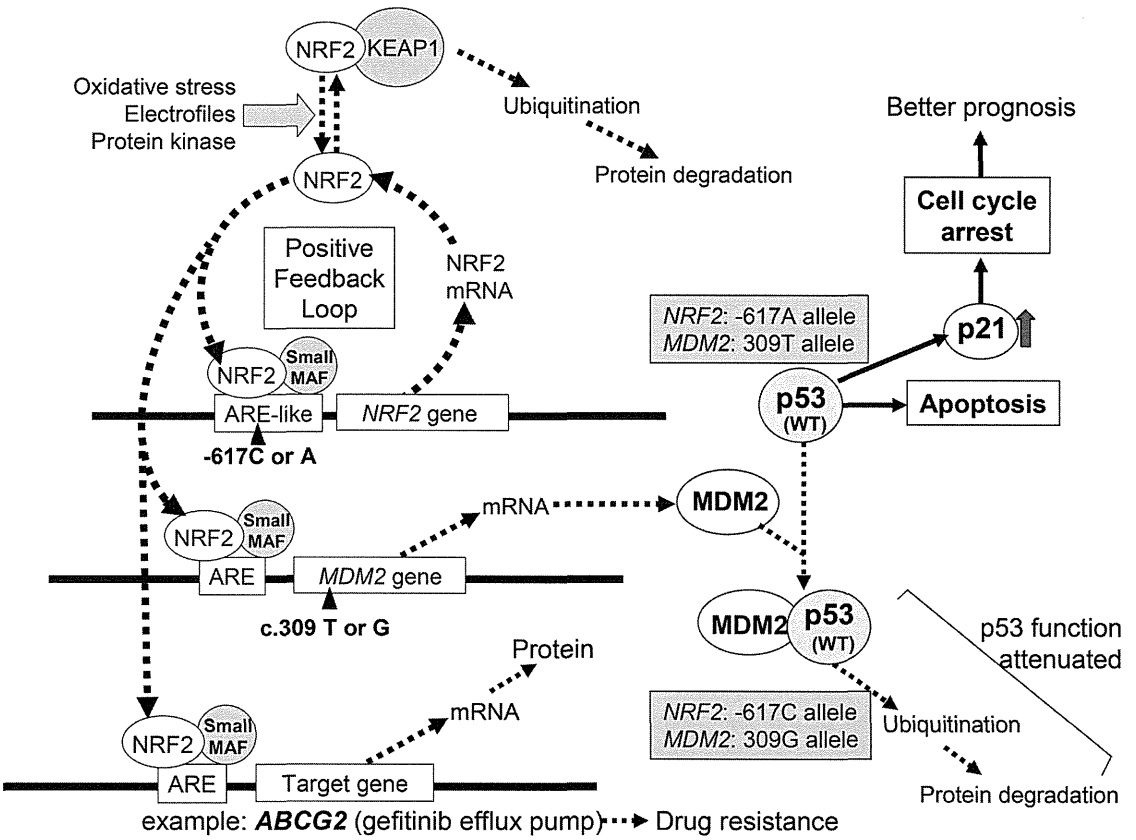

Figure 3. Schematic illustration showing the effect of *NRF2* SNP–617C>A and *MDM2* SNP c.309 T>G on the p53-mediated suppression of cancer cell proliferation and drug resistance. In response to oxidative stress, electrophiles challenge, or protein kinase-mediated phosphorylation (*e.g.*, via the PI3K-Akt pathway), the NRF2 protein is released from KEAP1 and then translocated into the nuclei. The SNP–617C>A in the ARE-like motif is considered to play a role in the positive feedback loop of transcriptional activation of the *NRF2* gene. The SNP homozygote (–617 A/A) significantly attenuates the positive feedback loop and also expression of NRF2-target genes, such as *MDM2* and *ABCG2*. In the case of *MDM2* gene expression, the SNP (c.309 T>G) in the first intron of the *MDM2* gene increases the binding affinity toward Sp1 and results in higher expression levels of MDM2 protein. MDM2 protein, thus highly expressed, binds to p53 (wild type; Wt) protein and leads to ubiquitination and proteasomal degradation of p53 (Wt) protein. Combination of the 309G (SNP) allele of the *MDM2* gene and the –617C (Wt) allele of the NRF2 gene may have negative impacts on p53 (Wt)-mediated tumor suppression. On the other hand, lung cancer patients harboring both the 309T (Wt) allele of the *MDM2* gene and the –617A (SNP) allele of the *NRF2* gene may have better prognosis due to the tumor suppressor function of p53 (Wt), such as apoptosis and $p21^{WAF1/cip1}$-mediated cell cycle arrest. Expression of the *ABCG2* gene is known to be up-regulated by NRF2. Gefitinib, an inhibitor of EGFR tyrosine kinase, is extruded by ABCG2 out of cancer cells. Thus, NRF2-mediated induction of ABCG2 expression can confer cancer cells with acquired resistance to gefitinib and other anticancer drugs.
doi:10.1371/journal.pone.0073794.g003

cell cycle arrest and/or apoptosis mediated by p53 (WT); refer to Figure 3. This may explain, in part, our finding that the lung cancer patients with homozygous SNP alleles (–617A/A) in the *NRF2* gene had markedly high overall survival rates (Figure 2).

In cancer tissues, somatic mutations take place frequently. In addition to the above-mentioned genetic polymorphisms as the "intrinsic" mechanism, mutations in the *KEAP1* and/or *NRF2* genes are the "acquired" mechanisms that lead to constitutive activation of NRF2. In fact, mutations in the *NRF2* and *KEAP1* genes have been found in carcinomas of the lung [12], breast [48], liver [49], and stomach [49]. Abnormalities in NRF2 activity were correlated with poor prognosis, when measured either as recurrence-free or overall 5-year survival. A recent immunohistochemical study has revealed that increased expression of NRF2 protein and decreased expression of KEAP1 protein are common abnormalities in NSCLC and are associated with poor prognosis [50]. Importantly, abnormal expression of NRF2 and KEAP1 proteins was more common than that of the corresponding gene mutaions [50], suggesting the involvement of other mechanisms such as intrinsic genetic polymorphisms of those genes. To bridge the gap between the homozygous SNP alleles (–617A/A) in the *NRF2* gene and the high overall survival of lung cancer patients shown in this study, we need to carry out further clinical follow-up studies with lung cancer patients (p-stages III and IV) who have been subjected to chemotherapeutic treatments. As exemplified in the present study, genetic polymorphisms/mutations and fine balances among NRF2, KEAP1, MDM2, p53, $p21^{WAF1/cip1}$ and other genes are likely to contribute to the progression of cancer and, consequently, the prognosis of cancer patients.

Development of a Rapid Genotyping Method for Personalized Cancer Therapy

One of the challenges in lung cancer management is to identify biomarkers for personalized cancer therapy. To effectively advance personalized medicine, cost-effective methods should be developed for genotyping. It would be desirable to include such

information in each patient's record as guidance for medial doctors to provide individualized treatment. In the present study, we have developed a rapid genetic testing method to elucidate the impact of genetic polymorphisms in the *NRF2* gene on the risk and survival of patients with primary lung cancer. The method enables the detection of genetic polymorphisms in target genes within 30 to 45 minutes under isothermal conditions that do not require DNA isolation and PCR amplification. Thus, this genotyping method would provide a simple and practical tool for personalized cancer therapy and assessment of prognosis.

Materials and Methods

Patients and Sample Collection

This clinical research was conducted according to the Declaration of Helsinki Principles. Under written informed consent, we collected blood samples from patients with primary lung cancer who received surgical operation at the Kanagawa Cancer Center. Protocols for sample collection, anonymity, storage, and transportation to RIKEN Yokohama Institute required for the present study were approved by both the Institutional Review Board of the Kanagawa Cancer Center Research Institute and the Research Ethics Committee at RIKEN Yokohama Institute. Procedures for analyzing the *HO-1* gene 5′-flanking region sequence as well as for genotyping the *NRF2*, *CYP2A6*, and *MDM2* genes in the genomic DNA samples were approved by the Research Ethics Committee at RIKEN Yokohama Institute.

The Taiwanese samples (N = 168) used in this study were randomly selected from the Han- Chinese Cell and Genome Bank in Taiwan described previously [51], in which more than 3,300 healthy controls were collected and randomly selected through registry.

Preparation of Genomic DNA

Peripheral venous blood samples from lung cancer patients were collected into tubes containing Na_2EDTA. Genomic DNA was extracted by the use of the QIAamp blood kit (QIAGEN K.K., Tokyo, Japan) according to the manufacturer's instructions.

Genotyping

Based on the SmartAmp method, rapid genotyping primers were developed for detecting both the SNP (c.–617C/A) in the ARE-like loci of the human *NRF2* gene (Figure 1) and the *CYP2A6*4* genotype (whole gene deletion) [51]. We used exciton-controlled hybridization-sensitive fluorescent primers for optical detection of genotyping reactions (Figure 1). After genomic DNA was denatured at 98°C for 3 min, the genotyping reactions were allowed to proceed isothermally at 60°C for 60 min in a Mx3000P PCR system (Agilent Technologies, Santa Clara, CA, USA). The SNP c.309T>G in of the *MDM2* gene were detected by the Duplex SmartAmp method, as described previously [46].

Analysis of Length Variability of $(GT)_n$ Repeats in the *HO-1* Gene Promoter

The partial genomic DNA including $(GT)_n$ repeats located in the 5′-flanking region of the *HO-1* gene was amplified by the polymerase chain reaction (PCR) [53,54] with a fluorescence probe-labeled sense primer p1-s (5′-AGAGCCTGCAGCTTCT-CAGA-3′) and an unlabeled anti-sense primer p1-as (5′-ACAAAGTCTGGCCATAGGAC-3′). These primers were designed according to the previously reported sequences [55]. The PCR cycle program of 95°C for 30 seconds, 63°C for 30 seconds, and 60°C for 30 seconds was carried out for a total of 30 cycles. The resulting PCR products were visualized by electrophoresis in 3% agarose gels containing ethidium bromide. The electrophoresis revealed two differently-sized PCR products attributable to two alleles with different $(GT)_n$ repeat sequences in the *HO-1* gene. The $(GT)_n$ repeats in the PCR products were analyzed with a laser-based automated DNA sequencer (ABI PRISM 3100 DNA Analyzer, Applied Biosystems Ltd., Tokyo, Japan).

Analysis of Mutation Status in the *EGFR* Gene

DNA samples were isolated from frozen tissues or formalin-fixed and paraffin-embedded tissue sections that had been surgically excised from lung cancer loci. Epidermal growth factor receptor (*EGFR*) gene exons 19 and 21 were analyzed for their mutational status by the loop-hybrid mobility shift assay, a PCR-based heteroduplex analysis method, as described previously [56,57].

Statistical Analysis

The association of lung cancer with the allele frequency of the gene of interest was assessed by considering the confounding effects derived from known risk factors, such as age, gender, smoking history, and histopathology. After preliminary bivariate analysis by using Fisher's exact test or χ^2test, the multivariate logistic regression method was performed to estimate independent variables associated with the SNP homozygote (–617A/A) in the *NRF2* gene. Furthermore, the Kaplan-Meier method was used to estimate survival curves for overall survival. Log-rank tests were used to compare the survival curves of patients in different *NRF2* subgroups. The statistical significance of all the data was tested by the analysis of variance. We performed statistical analysis with the SPSS statistics program (v.19.0; SPSS Inc., Chicago, USA). Values of $P<0.05$ were considered to indicate statistical significance.

Supporting Information

Table S1 Classification of female adenocarcinoma patients with respect to genotypes of *NRF2* and *MDM2* genes.
(DOC)

Acknowledgments

The authors thank Dr. Taisei Mushiroda (RIKEN Center for Integrative Medical Sciences) for his kind advice on the ethnic difference of NRF2 genotypes. In addition, thanks go to members of the SmartAmp team for their generous support in performing the DNA sequencing experiments at RIKEN Omics Science Center.

Author Contributions

Conceived and designed the experiments: YO UN AL YI YN TK YH. Performed the experiments: YO UN YE AL HK. Analyzed the data: YO TI SM MT. Contributed reagents/materials/analysis tools: YO UN YE AL HK. Wrote the paper: YO TI. Wrote the research plan: TI. Contributed to the sample collection: YM HN MTML TY. Contributed to the clinical study: YM HN MTML TY.

References

1. Centers for Disease Control and Prevention (CDC) website. Available: http://www.cdc.gov/cancer/lung/basic_info/risk_factors.html. Accessed 2013 Feb 10.
2. National Cancer Institute (NCI) website. Available: http://www.cancer.gov/cancertopics/types/lung. Accessed 2013 Feb 10.

3. Stämpfli MR, Anderson GP (2009) How cigarette smoke skews immune responses to promote infection, lung disease and cancer. Nature Reviews 9: 377–84.
4. Motohashi H, Yamamoto M (2004) Nrf2-Keap1 defines a physiologically important stress response mechanism. Trends Mol Med 10: 549–57.
5. Kobayashi M, Yamamoto M (2006) Nrf2-Keap1 regulation of cellular defense mechanisms against electrophiles and reactive oxygen species. Adv Enzyme Regul 46: 113–40.
6. Nguyen T, Nioi P, Pickett CB (2009) The Nrf2-antioxidant response element signaling pathway and its activation by oxidative stress. J Biol Chem 284: 13291–5.
7. Lau A, Villeneuve NF, Sun Z, Wong PK, Zhang DD (2008) Dual roles of Nrf2 in cancer. Pharmacol Res 58: 262–70.
8. Homma S, Ishii Y, Morishima Y, Yamadori T, Matsuno Y, et al. (2009) Nrf2 enhances cell proliferation and resistance to anticancer drugs in human lung cancer. Clin Cancer Res 15: 3423–32.
9. Hayes JD, McMahon M (2009) *NRF2* and *KEAP1* mutations: permanent activation of an adaptive response in cancer. *Trends* Biochem Sci 34: 176–88.
10. Taguchi K, Motohashi H, Yamamoto M (2011) Molecular mechanisms of the Keap1-Nrf2 pathway in stress response and cancer evolution. Genes Cells 16: 123–40.
11. Yamadori T, Ishii Y, Homma S, Morishima Y, Kurishima K, et al. (2012) Molecular mechanisms for the regulation of Nrf2-mediated cell proliferation in non-small-cell lung cancers. Oncogene 31: 4768–77.
12. Sporn MB, Liby KT (2012) NRF2 and cancer: the good, the bad and the importance of context. Nature Rev Cancer 12: 564–71.
13. Moi P, Chan K, Asunis I, Cao A, Kan YW (1994) Isolation of NF-E2-related factor 2 (Nrf2), a NF-E2-like basic leucine zipper transcriptional activator that binds to the tandem NF-E2/AP1 repeat of the beta-globin locus control region. Proc Natl Acad Sci U S A 91: 9926–30.
14. Itoh K, Wakabayashi N, Katoh Y, Ishii Y, Igarashi K, et al. (1999) Keap1 represses nuclear activation of antioxidant responsive elements by Nrf2 through binding to the amino-terminal Neh2 domain. Genes Dev 13: 76–86.
15. Itoh K, Igarashi K, Hayashi N, Nishizawa M, Yamamoto M (1995) Cloning and characterization of a novel erythroid cell-derived CNC family transcription factor heterodimerizing with the small Maf family proteins. Mol Cell Biol 15: 4184–93.
16. Ishii T, Itoh K, Takahashi S, Sato H, Yanagawa T, et al. (2000) Transcription factor Nrf2 coordinately regulates a group of oxidative stress-inducible genes in macrophages. J Biol Chem 275: 16023–9.
17. Ramos-Gomez M, Kwak MK, Dolan PM, Itoh K, Yamamoto M, et al. (2001) Sensitivity to carcinogenesis is increased and chemoprotective efficacy of enzyme inducers is lost in nrf2 transcription factor-deficient mice. Proc Natl Acad Sci USA 98: 3410–5.
18. Cho HY, Reddy SP, DeBiase A, Yamamoto M, Kleeberger SR (2005) Gene expression profiling of NRF2-mediated protection against oxidative injury. Free Radic Biol Med 38: 325–43.
19. Kwak MK, Itoh K, Yamamoto M, Kensler TW (2002) Enhanced expression of the transcription factor Nrf2 by cancer chemopreventive agents: role of antioxidant response element-like sequences in the nrf2 promoter. Mol Cell Biol 22: 2883–92.
20. Mitsuishi Y, Taguchi K, Kawatani Y, Shibata T, Nukiwa T, et al. (2012) Nrf2 redirects glucose and glutamine into anabolic pathways in metabolic reprogramming. Cancer Cell 22: 66–79.
21. Yamamoto T, Yoh K, Kobayashi A, Ishii Y, Kure S, et al. (2004) Identification of polymophisms in the promoter region of the human NRF2 gene. Biochem Biophys Res Commun 321: 72–9.
22. Marzec JM, Christie JD, Reddy SP, Jedlica AE, Vuong H, et al. (2007) Functional polymorphisms in the transcription factor *NRF2* in humans increase the risk of acute lung injury. FASEB 21: 2237–46.
23. Nakata K, Tanaka Y, Nakano T, Adachi T, Tanaka H, et al. (2006) Nuclear receptor-mediated transcription regulation in phase I, II, and III xenobiotic metabolizing systems. Drug Metab Pharmacokinet 21: 437–57.
24. Shen G, Kong AN (2009) Nrf2 plays an important role in coordinated regulation of phase II drug metabolism enzymes and phase III drug transporters. Biopharm Drug Dispos 30: 345–55.
25. Adachi T, Nakagawa H, Chung I, Hagiya Y, Hoshijima K, et al. (2007) Nrf2-dependent and -independent induction of ABC transporters ABCC1, ABCC2, and ABCG2 in HepG2 cells under oxidative stress. J Exp Ther Oncol 6: 335–48.
26. Sing A, Wu H, Zhang P, Happel C, Ma J, et al. (2010) Expression of *ABCG2 (BCRP)* is regulated by Nrf2 in cancer cells that confers side population and chemoresistance phenotype. Mol Cancer Ther 9: 2365–76.
27. Mitani Y, Lezhava A, Kawai Y, Kikuchi T, Oguchi-Katayama A, et al. (2007) Rapid SNP diagnostics using asymmetric isothermal amplification and a new mismatch-suppression technology. Nat Methods 4: 257–62.
28. Ishikawa T, Hayashizaki Y (2013) Clinical SNP detection by SmartAmp method. Methods Mol Biol 1015: 55–69.
29. Travis WD, Brambilla E, Müller-Hermelink HK, Harris CC (2004) Pathology and genetics of tumours of the lung, pleura, thymus and heart. Lyon, France: IARC Press.
30. Hsiung CA, Lan Q, Hong YC, Chen CJ, Hosgood HD, et al. (2010) The 5p15.33 locus is associated with risk of lung adenocarcinoma in never-smoking females in Asia. PLoS Genet 6: pii: e1001051.
31. Hosgood HD 3rd, Wang WC, Hong YC, Wang JC, Chen K, et al. (2012) Genetic variant in TP63 on locus 3q28 is associated with risk of lung adenocarcinoma among never-smoking females in Asia. Hum Genet. 131: 1197–203.
32. Lan Q, Hsiung CA, Matsuo K, Hong YC, Seow A, et al. (2012) Genome-wide association analysis identifies new lung cancer susceptibility loci in never-smoking women in Asia. Nature Genet 44: 1330–5.
33. Toyooka S, Matsuo K, Shigeharu H, Kosaka T, Tokumo M, et al. (2007) The impact of sex and smoking status on the mutational spectrum of epidermal growth factor receptor gene in non small cell lung cancer. Clin Cancer Res 13: 5622–5.
34. Ladanyi M, Pao W (2008) Lung adenocarcinoma: guiding EGFR-targeted therapy and beyond. Mod Pathol 21 Suppl 2: S16–22.
35. Fukuoka M, Wu YL, Thongprasert S, Sunpaweravong P, Leong SS, et al. (2011) Biomarker analyses and final overall survival results from a phase III, randomized, open-label, first-line study of gefitinib versus carboplatin/paclitaxel in clinically selected patients with advanced non-small-cell lung cancer in Asia (IPASS). J Clin Oncol 29: 2866–74.
36. Paez JG, Jänne PA, Lee JC, Tracy S, Greulich H, et al. (2004) EGFR mutations in lung cancer: correlation with clinical response to gefitinib therapy. Science 304: 1497–500.
37. Lynch TJ, Bell DW, Sordella R, Gurubhagavatula S, Okimoto RA, et al. (2004) Activating mutations in the epidermal growth factor receptor underlying responsiveness of non-small-cell lung cancer to gefitinib. N Engl J Med 350: 2129–39.
38. Pao W, Miller V, Zakowski M, Doherty J, Politi K, et al. (2004) EGF receptor gene mutations are common in lung cancers from "never smokers" and are associated with sensitivity of tumors to gefitinib and erlotinib. Proc Natl Acad Sci U S A 101: 13306–11.
39. Saito H, Hirano H, Nakagawa H, Fukami T, Oosumi K, et al. (2006) A new strategy of high-speed screening and quantitative structure-activity relationship analysis to evaluate human ATP-binding cassette transporter ABCG2-drug interactions. J Pharmacol Exp Ther 317: 1114–24.
40. Meyer zu Schwabedissen HE, Grube M, Dreisbach A, Jedlitschky G, Meissner K, et al. (2006) Epidermal growth factor-mediated activation of the map kinase cascade results in altered expression and function of ABCG2 (BCRP). Drug Metab. Dispos. 34: 524–33.
41. Huang WC, Chen YJ, Li LY, Wei YL, Hsu SC, et al. (2011) Nuclear translocation of epidermal growth factor receptor by Akt-dependent phosphorylation enhances breast cancer-resistant protein expression in gefitinib-resistant cells. J. Biol. Chem. 286: 20558–68.
42. You A, Nam CW, Wakabayashi N, Yamamoto M, Kensler TW, et al. (2011) Transcriptional factor Nrf2 maintains the basal expression of Mdm2: An implication of the regulation of p53 signaling by Nrf2. Arch Biochem Biophys 507: 356–364.
43. Freedman DA, Wu L, Levine AJ (1999) Functions of the MDM2 oncoprotein. Cell Mol Life Sci 55: 96–107.
44. Rotblat B, Melino G, Knight RA (2012) NRF2 and p53: Januses in cancer? Oncotarget 3: 1272–1283.
45. Bond GL, Hu WW, Bond EE, Robins H, Lutzker SG, et al. (2004) A single nucleotide polymorphism in the MDM2 promoter attenuates the p53 tumor suppressor pathway and accelerates tumor formation in humans. Cell 119: 591–602.
46. Enokida Y, Shimizu K, Atsumi J, Lezhava A, Tanaka Y, et al. (2013) Rapid detection of SNP (c.309T>G) in the MDM2 gene by the Duplex SmartAmp method. PLoS One. 8: e60151.
47. Han JY, Lee GK, Jang DH, Lee SY, Lee JS (2008) Association of p53 codon 72 polymorphism and MDM2 SNP309 with clinical outcome of advanced nonsmall cell lung cancer. Cancer 113: 799–807.
48. Sjöblom T, Jones S, Wood LD, Parsons DW, Lin J, et al. (2006) The consensus coding sequences of human breast and colorectal cancers. Science 314: 268–74.
49. Yoo NJ, Kim HR, Kim YR, An CH, Lee SH (2012) Somatic mutations of the *KEAP1* gene in common solid cancers. Histopathology 60: 943–52.
50. Solis LM, Behrens C, Dong W, Suraokar M, Ozburn NC, et al. (2010) Nrf2 and Keap1 abnormalities in non-small cell lung carcinoma and association with clinicopathologic features. Clin Cancer Res 16: 3743–53.
51. Pan WH, Fann CS, Wu JY, Hung YT, Ho MS, et al. (2006) Han Chinese cell and genome bank in Taiwan: purpose, design and ethical considerations. Hum Hered 61: 27–30.
52. Azuma K, Lezhava A, Shimizu M, Kimura Y, Ishizu Y, et al. (2011) Direct genotyping of *Cytochrome P450 2A6* whole gene deletion from human blood samples by the SmartAmp method. Clin Chim Acta 412: 1249–51.
53. Kimpara T, Takeda A, Watanabe K, Itoyama Y, Ikawa S, et al. (1997) Microsatellite polymorphism in the human heme oxygenase-1 gene promoter and its application in association studies with Alzheimer and Parkinson disease. Hum Genet 100: 145–7.
54. Okinaga S, Takahashi K, Takeda K, Yoshizawa M, Fujita H, et al. (1996) Regulation of human heme oxygenase-1 gene expression under thermal stress. Blood 87: 5074–84.
55. Shibahara S, Sato M, Muller RM, Yoshida T (1989) Structural organization of the human heme oxygenase gene and the function of its promoter. Eur J Biochem 179: 557–63.
56. Oshita F, Matsukuma S, Yoshihara M, Sakuma Y, Ohgane N, et al. (2006) Novel heteroduplex method using small cytology specimens with a remarkably

high success rate for analysing EGFR gene mutations with a significant correlation to gefitinib efficacy in non-small-cell lung cancer. Br J Cancer 95: 1070–5.

57. Matsukuma S, Yoshihara M, Kasai F, Kato A, Yoshida A, et al. (2006) Rapid and simple detection of hot spot point mutations of epidermal growth factor receptor, BRAF, and NRAS in cancers using the loop-hybrid mobility shift assay. J Mol Diagn 8: 504–12.

Achievement of protein micro-crystallography at SPring-8 beamline BL32XU

2013 J. Phys.: Conf. Ser. 425 012002

(http://iopscience.iop.org/1742-6596/425/1/012002)

Journal of Physics: Conference Series **425** (2013) 012002 doi:10.1088/1742-6596/425/1/012002

Achievement of protein micro-crystallography at SPring-8 beamline BL32XU

Kunio Hirata[1], Yoshiaki Kawano[1], Go Ueno[1], Koichi Hashimoto[1], Hironori Murakami[1], Kazuya Hasegawa[2], Takaaki Hikima[1], Takashi Kumasaka[1] and Masaki Yamamoto[1]*

[1]RIKEN/SPring-8 Center 1-1-1 Kouto, Sayo-cho, Sayo-gun, Hyogo 679-5148, Japan

[2]JASRI/SPring-8 1-1-1 Kouto, Sayo-cho, Sayo-gun, Hyogo 679-5148, Japan

E-mail of the corresponding author: yamamoto@riken.jp

Abstract. A micro-focused X-ray beam with size ranging from 1 x 1 to 10 x 10 μm has been achieved at beamline BL32XU at SPring-8, Japan. Combining the available micro-beam with newly developed techniques has enabled efficient protein micro-crystallography.

1. Introduction

Recently, micro-focus X-ray beams have been proven to be effective for protein micro-crystallography [1]. The micro-focused beam enhances the signal-to-noise (S/N) ratio of diffraction peaks and reduces background noise from the non-crystal irradiated volume. Several beamlines worldwide have achieved a beamsize smaller than 10 μm for this purpose. The dedicated protein micro-crystallography beamline BL32XU at SPring-8 has been developed in the Japanese National Project, Targeted Protein Research Program. The concept of this beamline was described in our previous proceeding of SRI2009 [2]. By the end of 2009, we had completed the beamline commissioning and had achieved 1 μm focusing at the sample position. Since 2010, through two years of user operation, efficient methodologies for diffraction experiments using micro-beams have been developed.

In this manuscript, we describe achievements in protein micro-crystallography at BL32XU focusing on beamline capabilities, data collection strategy, enhancing S/N ratio and high speed screening for tiny protein crystals.

2. Fundamental abilities of the beamline BL32XU

The beamline consists of a primary slit, a monochromator, four-bladed slit for producing a virtual source, focusing K-B mirror and diffractometer [2]. A set of elliptically-shaped mirrors were fabricated with Elastic Emission Machining technique. Their demagnification factors for the horizontal and vertical directions correspond to 40 and 26, respectively. By producing a 40(H) and 26(V) μm aperture with the four-bladed slit, a 1 μm focused beam can be achieved. The minimum beam size is 0.9 x 0.9 μm with a corresponding flux of 6.2 x 10^{10} photons/sec at 12.4 keV [Fig.1]. A comparable photon flux density is available over the energy range 8.5 to 18.0 keV. The maximum beam size is 10 x 10 μm with 5.4 x 10^{12} photons/sec at 12.4 keV, achieved by setting the four-bladed slit to the fully open position. Modifying the slit aperture enables selection of beam shape and size from 1 x 1 μm to 10 x 10 μm within 15 seconds.

3. User friendly GUI system for suggesting data collection strategy

We have been developing the 'KUMA' GUI software, with the capability to suggest data collection strategies for reduced radiation damage. A recommended data collection method at BL32XU is so-called 'helical data collection' [3] using 1(H) x 10(V) μm beam. We measured the propagation length of radiation damage on standard protein crystals at various X-ray energies and beam sizes, as reported by APS staff [4]. From the results, an empirical model function estimating the accumulated dose on the crystal was established. Using this model, KUMA suggests an optimal strategy taking into account X-ray energy, crystal size, beam size, desired data redundancy and aimed quantity of dose [to be published]. The KUMA system enables users to make the maximum use of crystal volume for data collection. Several successful structure determinations from tiny lipidic cubic phase (LCP) crystals proved the efficiency of this system. In the case described in reference [5], helical data collection using a 1(H) x 10(V) μm beam and 0.5 μm step was conducted. The total absorbed dose was kept below 5 MGy for each of three MAD datasets by using this concept.

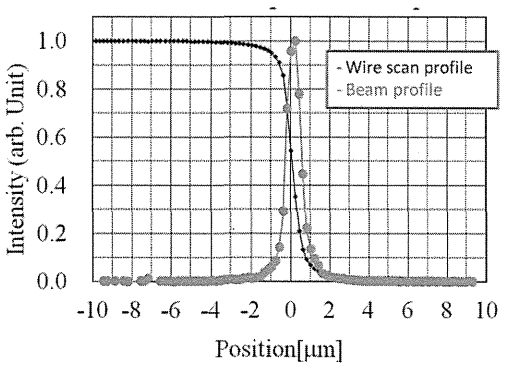

Figure 1.
Vertical beam profile. The profile was measured with a knife edge scan. The FWHM corresponded to 0.9 μm in both the vertical and horizontal directions.

4. Developments for enhancing S/N ratio in data collection

It is exceedingly important for enhancing S/N ratio to reduce background noise originating from both air and parasite scattering. A high-precision diffractometer and newly developed helium gas chamber have been installed into the end-station of BL32XU.

4.1. Diffractometer

At beamline BL32XU, a pinhole collimator located 25 mm upstream of the sample position cuts off both parasitic scattering from mirrors and air. The pinhole diameter of 30 μm can cover the utilized beam sizes. The scattering from the pinhole is reduced by a 10 mm-long brass pipe with a diameter of 300 μm.

A key component for data collection from tiny protein crystals is the crystal goniometer. We adopted an air-bearing goniometer having a sphere of confusion of less than 0.5 μm (KOHZU Precision Co., Ltd.). The minimum step resolution of each crystal translation axis corresponds to 0.1 μm. The absolute position of each translational axis can be monitored with the linear encoder (RENISHAW) with a resolution of 10 nm.

4.2. Helium chamber

We have developed a helium gas chamber, now available to users, for reducing the air scattering along the beam path (Figure 2(a)). The rigid part of the chamber consists of acrylic plates and encloses all devices around the sample position. A paper-made bellows part connects the acrylic box with the CCD detector surface. Helium gas is introduced into the chamber using a helium cryo-stream at a defined temperature between 30-100 K. With the chamber in place, the detector to sample distance may be set between 180-500 mm. The chamber was designed so that our sample changer robot, SPACE [6], can access sample pins on the goniometer with minimal loss of helium gas from the chamber. A small door, the so-called 'cat flap', was installed in the rigid part of the chamber and the arm of the SPACE robot opens this door when it exchanges sample pins (Figure 2(b)).

With this system, the user can conduct diffraction experiments in a similar manner as in routine data collection. The helium environment has been confirmed to reduce background noise from air scattering by a factor of 10 at 12.4 keV [Figure 2(c)]. One user experiment at this X-ray energy demonstrated that even an incident beam attenuated to 25% gave the same quality of diffraction dataset as the normal setting, which utilizes nitrogen gas flow.

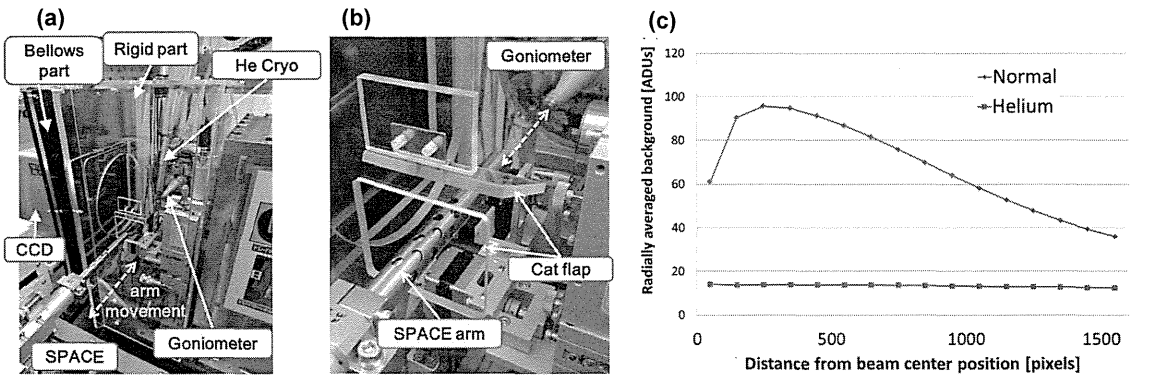

Figure 2. (a) The overall view of the helium chamber. The X-ray beam travels from right to left. The goniometer and other devices around the sample are enclosed by the rigid part made of acrylic plates. The paper-made bellows part connects the rigid part and X-ray CCD detector. (b) The function of the 'cat flap'. The sample changer robot, SPACE, can gain access to the goniometer head through a small hinged door, the 'cat flap'. SPACE can exchange sample pins via this door with a very small change of helium gas concentration in the chamber. (c) Radially averaged background ADUs with and without helium chamber. The 'normal' trace shows background without the helium chamber. Both images were acquired using an exposure of 5 x 10^{11} photons at 12.4 keV. The detector was a Rayonix MX225HE and the camera length was set to 300 mm from the sample position with an offset ADU of 10. The inner 200 pixel-length region was affected by the direct beam stopper.

5. Plate screening for micro crystals

In protein crystallography, obtaining a good quality crystal is an essential yet challenging step. Therefore, huge numbers of crystallization conditions are tried in the initial screening process and a number of small objects are often observed in these crystallization drops. However, it is difficult to establish whether these are protein crystals or not. In particular, crystals obtained with the LCP (lipidic cubic phase) method [7] often do not grow large enough to give high quality diffraction. Such crystals are easily deformed in the freezing process for cryo-crystallography because the phase condition of the lipid is very sensitive to variations of humidity and temperature. Furthermore, a major difficulty with LCP crystals is that LCP becomes opaque upon freezing and hence it is very difficult to visually align crystals. For these reasons, there is strong user demand for an *in-situ* crystal screening system at room temperature using X-rays [8].

We have developed an *in-situ* plate screening system at beamline BL32XU dedicated to the standard SBS-format crystallization plate, mounted manually (Figure 3(a)) (KOHZU Precision Co., Ltd.). Installation of this equipment is carried out exclusively using the goniometer stage and cryogenic equipment, with no other disturbance to the beamline. This system has three translation axes, with a positional repeatability of 1 μm, to cover the whole area of the SBS plate. The area covered with these translational axes is 25 x 120 x 100 mm with a maximum scan speed of 1.5 mm/sec.

An *in-situ* plate screening system for LCP crystals was also developed. For this system, the translation axes are equipped onto the goniometer (Figure 3(b)) (RIGAKU Aihara Precision Co., Ltd.). It can be more easily mounted than the SBS system described above. To utilize this system, the crystallization plate is required to be cut and mounted on a standard 25 x 75 mm glass slide. Oscillation images can be also collected using the spindle axis of the goniometer.

By combining these systems with an X-ray CMOS detector [9], it is possible to scan whole one well area within one minute. In our trial experiment, 3Å resolution diffraction spots were obtained from hen egg white lysozyme crystals smaller than 10 μm.

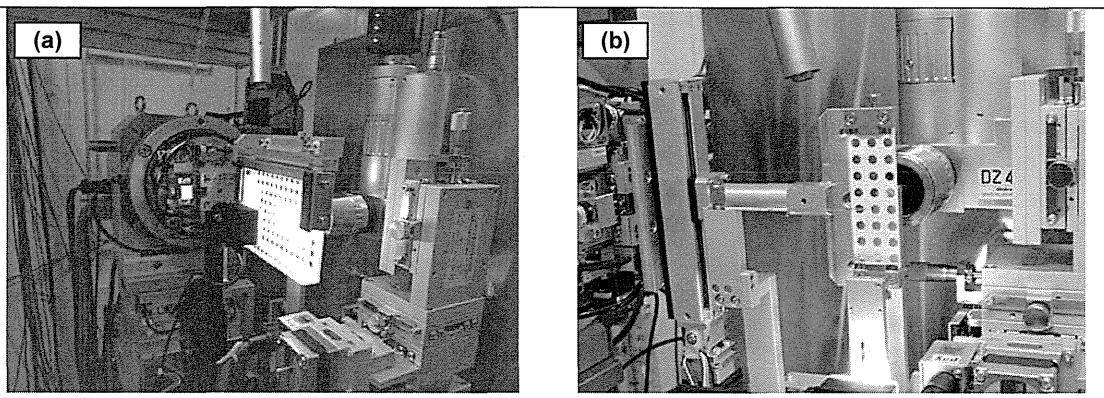

Figure 3. *in-situ* plate screening systems developed at BL32XU (a) For the standard SBS-format crystallization plate (b) For a standard slide glass size of 25 x 75 mm dedicated to LCP crystals

6. Challenges for automatic detection of protein micro-crystals

Generally, it is difficult to visualize tiny protein crystals because the refractive indices of the protein crystal and mother liquor are similar. We have developed an optical system to visualize such invisible protein crystals. The concept of this system is to visualize fluorescently labeled protein micro-crystals using an excitation light source and a modified co-axial microscope with emission filters currently installed on the beamline. Utilized fluorescent dyes include DyLight350 (Thermo Scientific Co., Ltd), FITC (fluorescein isothiocyanate), TAMRA (Carboxytetramethylrhodamine) and Cy5 [10]. The emission filter and excitation light source are manually changed according to the type of fluorescent dyes. Post-crystallization soaking with fluorescent labels was successful without detectable changes to crystal shape or diffraction data quality.

A newly developed program coded with C++ and OpenCV library has enabled automatic recognition of fluorescently labeled protein crystals. The positions of crystals are identified from digital images captured using a co-axial microscope. The program can interact with the beamline control system BSS [11] to quickly and easily position the identified crystal at the irradiation position for data collection.

7. Conclusion

We have achieved a focused X-ray beam of 1x1 μm with a flux of 6 x 10^{10} photons/sec at the beamline BL32XU at SPring-8. Combining this micro-beam with the integrated systems described in this manuscript has enabled users to conduct efficient data collection and crystal screening of protein micro-crystals.

References

[1] Rasmussen, S. G. F. *et al. Nature* **450**, 383–7 (2007).
[2] Hirata, K. *et al. AIP conf. proc.* **1234**, 901–904 (2010).
[3] Flot, D. *et al. J. Sync. Rad.* **17**, 107–118 (2010).
[4] Sanishvili, R. *et al. PNAS* **108**, 6127–32 (2011).
[5] Kato, H. E. *et al. Nature* **482**, 369–74 (2012).
[6] Murakami, H. *et al. J. Appl. Cryst.* **45**, 234–238 (2012).
[7] Landau, E. *et al. PNAS* **93**, 14532–14535 (1996).
[8] Axford, D. *et al. Acta Cryst.* **D68**, 592-600(2012)
[9] Hasegawa, K. *et al. J. Appl.Cryst.* **42**, 1165–1175 (2009).
[10] Ernst, L. *et al. Cytometry* **10**, 3–10 (1989).
[11] Ueno, G. *et al. J. Sync. Rad.* **12,** 380–384 (2005).

Development 140, 3221-3229 (2013) doi:10.1242/dev.094854

Molecular dissection of IZUMO1, a sperm protein essential for sperm-egg fusion

Naokazu Inoue[1,2], Daizo Hamada[3], Hironari Kamikubo[4], Kunio Hirata[5], Mikio Kataoka[4], Masaki Yamamoto[5], Masahito Ikawa[1], Masaru Okabe[1] and Yoshihisa Hagihara[6,*]

SUMMARY

Although the membrane fusion of spermatozoon and egg cells is the central event of fertilization, the underlying molecular mechanism remains virtually unknown. Gene disruption studies have showed that IZUMO1 on spermatozoon and CD9 on oocyte are essential transmembrane proteins in sperm-egg fusion. In this study, we dissected IZUMO1 protein to determine the domains that were required for the function of sperm-egg fusion. We found that a fragment of the N terminus (Asp5 to Leu113) interacts with fertilization inhibitory antibodies. It also binds to the egg surface and effectively inhibits fusion *in vitro*. We named this fragment 'IZUMO1 putative functional fragment (IZUMO1$_{PFF}$)'. Surprisingly, IZUMO1$_{PFF}$ still maintains binding ability on the egg surface of *Cd9*$^{-/-}$ eggs. A series of biophysical measurements using circular dichroism, sedimentation equilibrium and small angle X-ray scattering revealed that IZUMO1$_{PFF}$ is composed of an N-terminal unfolded structure and a C-terminal ellipsoidal helix dimer. Egg binding and fusion inhibition were not observed in the IZUMO1$_{PFF}$ derivative, which was incapable of helix formation. These findings suggest that the formation of a helical dimer at the N-terminal region of IZUMO1 is required for its function. Cos-7 cells expressing the whole IZUMO1 molecule bound to eggs, and IZUMO1 accumulated at the interface between the two cells, but fusion was not observed. These observations suggest that IZUMO1 alone cannot promote sperm-egg membrane fusion, but it works as a factor that is related to the cellular surface interaction, such as the tethering of the membranes by a helical region corresponding to IZUMO1$_{PFF\text{-}core}$.

KEY WORDS: Sperm-egg fusion, Membrane fusion, IZUMO1

INTRODUCTION

The membrane fusion of spermatozoon and oocyte is the central event of fertilization, where the genetic materials of two gametes merge. Despite the biological importance of this event, targeted deletion studies have revealed only two proteins, CD9 and IZUMO1, to be necessary in sperm-egg fusion (Primakoff and Myles, 2007). Although CD9 is a ubiquitously expressed protein, gene disruption resulted in infertile females but otherwise healthy mice. Subsequent experiments revealed that CD9 functions as an essential factor for sperm-egg fusion in eggs (Kaji et al., 2000; Le Naour et al., 2000; Miyado et al., 2000). We have previously identified a sperm-specific protein, IZUMO1, which is indispensable for mouse sperm-egg fusion (Inoue et al., 2005). In mice lacking either *Cd9* on eggs or *Izumo1* on spermatozoa, membrane fusion was almost completely impaired. To date, how these two proteins mediate membrane fusion is unclear and therefore the molecular mechanism behind of sperm-egg fusion remains virtually unknown.

IZUMO1 is a 377 amino acid type I transmembrane protein with a large extracellular region, a single transmembrane region and a short cytoplasmic tail. In this study, we focused on the 319 amino acid extracellular region of murine IZUMO1. Protein domain search programs (Zdobnov and Apweiler, 2001; McGuffin and Jones, 2003; Letunic et al., 2006) have identified only one immunoglobulin-like domain in the extracellular region. In addition, Ellerman et al. have found that three novel proteins (IZUMO2, IZUMO3 and IZUMO4) share a local sequence similarity with IZUMO1 (Ellerman et al., 2009). These proteins were characterized by the presence of a new sequence motif, called the Izumo domain, with a conserved cluster of eight cysteines: C-X(2)-C-X(106,108)-C-X(3,4)-C-X(9)-C-X(2)-C-X(6)-C-X(4,5)-C. However, it is unclear how these motifs are related to functions of IZUMO1 in sperm-egg fusion.

Here, we have first tried to clarify the functional site in IZUMO1 for sperm-egg fusion by using fusion-inhibiting monoclonal antibodies and a series of recombinant IZUMO1 fragments (Fig. 1). A fluoresceinated fragment that includes the potential functional site was incubated with zona-free eggs and was used to probe its affinity to eggs. In addition, recombinant IZUMO1 fragments were added to the *in vitro* fertilization system and were examined for their fusion inhibitory activities. The biophysical properties of the putative functional site of IZUMO1 were subsequently analyzed using circular dichroism (CD), sedimentation equilibrium and small angle X-ray scattering (SAXS). Combining the above functional and structural data, we discussed the putative molecular function of IZUMO1 in gamete fusion.

MATERIALS AND METHODS

All animal experiments were approved by the Animal Care and Use Committee of the Research Institute for Microbial Diseases, Osaka University, Japan.

Preparation of antibodies

Female rats were immunized with mouse sperm, and spleen cells were subjected to cell fusion with P3U1 cells. Indirect immunofluorescence

[1]Research Institute for Microbial Diseases, Osaka University, Yamadaoka 3-1, Suita, Osaka 565-0871, Japan. [2]Department of Cell Science, Institutes for Biomedical Sciences, School of Medicine, Fukushima Medical University, 1 Hikarigaoka, Fukushima City, Fukushima 960-1295, Japan. [3]Division of Structural Biology (GCOE), Department of Biochemistry and Molecular Biology, Graduate School of Medicine, Kobe University, 7-5-1 Kusunoki-cho, Chuo-ku, Kobe, Hyogo 650-0017, Japan. [4]Graduate School of Materials Science, Nara Institute of Science and Technology, Ikoma, Nara 630-0101, Japan. [5]SPring-8/RIKEN, Kouto, Sayo-gun, Hyogo 679-5148, Japan. [6]National Institute of Advanced Industrial Science and Technology (AIST), 1-8-31 Midorigaoka, Ikeda, Osaka 563-8577, Japan.

*Author for correspondence (hagihara-kappael@aist.go.jp)

Accepted 28 May 2013

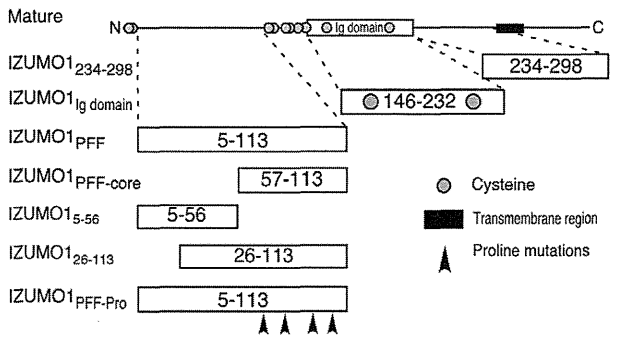

Fig. 1. Mouse mature IZUMO1 and fragments. The region of each fragment is shown by the position of the aligned blank bar, with the N- and C-terminal amino acid residue numbers inside the bar. The N-terminal amino acid sequence of native IZUMO1 was confirmed to be Cys-Ile-Lys-Cys-Asp. The fragments that were used in this work were numbered after the removal of signal peptides (from the first Met to the 21st Pro) from the pre-protein. Gray circles and filled bar in mature IZUMO1 indicate the cysteines and transmembrane region, respectively. There are two clusters of cysteines: at the distal N-terminal end and around residues 114-144. We prepared $IZUMO1_{PFF}$ and $IZUMO1_{PFF\text{-}core}$ with and without a His-tag and linker. In addition, the fragments with an additional cysteine and linker at the C terminus were also made for the conjugation of a fluorescent dye. $IZUMO1_{234\text{-}298}$, $IZUMO1_{5\text{-}56}$ and $IZUMO1_{26\text{-}113}$ have an additional nine amino acids containing a His-tag and linker.

staining as the first screening was employed (Okabe et al., 1987). Hybridomas expressing anti-IZUMO1 antibodies were then further selected by western blotting using a hybridoma culture as a source of primary antibodies. Each hybridoma culture was compared in terms of reactivity against proteins with a molecular weight of 56 kDa in the sperm extract.

Preparation of IZUMO1 fragments

DNA coding for the extracellular region of mouse IZUMO1 was constructed using synthetic DNA with codon use that was optimized for expression in *Escherichia coli*. IZUMO1 fragments were amplified by polymerase chain reaction (PCR) with a 3′-primer with and without sequence encoding Ala-Gly-Gly-His-His-His-His-His-His, a linker plus a hexahistidine tag. In addition, IZUMO1 fragments with the sequence encoding Gly-Gly-Gly-Gly-Ser-Cys were prepared for fluorescent labeling by thiol-maleimide coupling. $IZUMO1_{234\text{-}298}$ was designed to start from Pro233 with a His-tag and linker; however, the purified fragment lacked the first proline, as judged by matrix-assisted laser desorption ionization time-of-flight (MALDI-TOF) mass spectrometry. Amplified PCR products were cloned back into pAED4 (Doering and Matsudaira, 1996). In $IZUMO1_{PFF\text{-}Pro}$, Leu70, Leu81, Leu94 and Leu104 of $IZUMO1_{PFF}$ were mutated to prolines using PCR-based mutagenesis.

All constructs were expressed in *E. coli* strain BL21 (DE3) pLysS (Agilent Technologies, La Jolla, CA). $IZUMO1_{PFF}$ and $IZUMO1_{Ig\ domain}$ were strongly expressed and accumulated in inclusion bodies. Inclusion bodies from 1.6 l of culture medium were suspended in 3 ml of 10 mM Tris-HCl (pH 8.5) and were solubilized by the addition of 3 g of solid guanidine hydrochloride (GdnHCl). These samples were then purified over a Superdex 75 (GE Healthcare, Waukesha, WI) that was pre-equilibrated with 6 M urea in 10 mM Tris-HCl (pH 8.5). $IZUMO1_{234\text{-}298}$, $IZUMO1_{26\text{-}113}$ and $IZUMO1_{5\text{-}56}$ were recovered in the soluble fraction and were purified using a HiTrap metal-chelating column (GE Healthcare). Finally, all samples were purified using reverse-phase chromatography, except $IZUMO1_{234\text{-}298}$ and $IZUMO1_{PFF}$ variants with two or more cysteines. $IZUMO1_{234\text{-}298}$ was further purified by ion exchange chromatography. $IZUMO1_{PFF\text{-}core}$ was prepared from partially purified $IZUMO1_{PFF}$ by limited proteolysis using 1/500 (w/w) proteinase K (Merck KGaA, Darmstadt, Germany) at 10°C for 1.5-2 hours. Proteolyzed fragments were then applied to reverse-phase chromatography for final purification of $IZUMO1_{PFF\text{-}core}$.

MALDI-TOF mass spectrometry confirmed that the molecular weights of purified IZUMO1 fragments were identical to the expected values that were calculated from their amino acid sequences (with an error of ±0.025%). Protein stock concentrations were determined by measuring the absorbance at 280 nm in 6 M GdnHCl, 20 mM sodium phosphate (pH 6.5). Molar extinction coefficients were calculated based on the number of Trp and Tyr residues using the Edelhoch spectral parameters (Edelhoch, 1967) (supplementary material Table S1). In this article, the molar concentrations of IZUMO1 fragments were estimated by assuming that they are monomers in a solution.

Measurements of surface plasmon resonance spectra

The antibodies were immobilized to the CM-5 sensor chip by the amine coupling protocol that was supplied by the manufacturer at 25°C using Biacore 2000 (GE Healthcare). The surface plasmon resonance (SPR) spectra of the IZUMO1 fragments were measured in 10 mM HEPES, 150 mM NaCl, 3 mM EDTA and 0.005% Tween-20 at 20°C, and the bound fragments were washed with 10 mM glycine and 0.5 M NaCl at pH 2.0. All experiments were duplicated.

In vitro fertilization

Mouse spermatozoa were collected from the cauda epididymis and were capacitated *in vitro* for 2 hours in a 200 μl drop of TYH medium that was covered with paraffin oil. B6D2F1 female mice (>8 weeks old) were superovulated with an injection of 5 IU of human chorionic gonadotropin (hCG) 48 hours after a 5 IU injection of equine chorionic gonadotropin (eCG). The eggs were collected from the oviduct 14 hours after the hCG injection. Eggs were placed in a 200 μl drop of TYH medium. These eggs were incubated with 2×10^5 spermatozoa/ml for 2 hours at 37°C in 5% CO_2 with anti-IZUMO1 monoclonal antibodies, and unbound spermatozoa were washed away. Eggs were observed 24 hours after insemination for the two-cell development under a Hoffman modulation contrast microscope.

Sperm-egg fusion assay

B6D2F1 female mice (>8 weeks old) were superovulated with an injection of 5 IU of hCG 48 hours after a 5 IU injection of eCG. The eggs were collected from the oviduct 14 hours after the hCG injection. Eggs were placed in a 200 μl drop of TYH medium. After being freed from cumulus cells with 0.01% (w/v) hyaluronidase, the zona pellucida was removed from mouse eggs using a piezo-manipulator, as previously reported (Yamagata et al., 2002). Zona-free mouse eggs were preloaded with 1 μg/ml Hoechst 33342 (Life Technologies, CA, USA) in TYH medium for 10 minutes and were washed prior to the addition of the spermatozoon. Zona-free eggs were co-incubated with 2×10^5 mouse spermatozoa/ml for 30 minutes at 37°C in 5% CO_2 with and without antibodies or IZUMO1 fragments. After 30 minutes of incubation, the eggs were observed under a fluorescence microscope (UV excitation light) after fixing with 0.25% glutaraldehyde. This procedure enabled staining of only fused sperm nuclei by transferring the dye into spermatozoa after membrane fusion.

Assay for the binding of IZUMO1 fragments to mouse eggs

Mouse zona-free eggs (wild type and $Cd9^{-/-}$) were prepared as above. Eggs were incubated with 3 μM IZUMO1 fragments that were fluoresceinated with Alexa Fluor 546 (Life Technologies) and 1 μg/ml of Hoechst 33342 for 2 hours at 37°C in TYH medium. After the eggs had been washed twice in TYH medium for 5 minutes each, the eggs were observed. For these experiments, especially careful preparation of zona-free eggs was required to avoid the occasional aberrant strong staining of eggs by fluoresceinated fragments. We used an FV-1000 microscope (Olympus, Tokyo, Japan) to obtain the confocal images.

Biophysical measurements

CD spectroscopy was performed using a J-820 spectropolarimeter (Jasco, Tokyo, Japan) with a 1 mm cell at 20°C in 10 mM Tris-HCl (pH 8.5) buffer. CD spectra were measured at protein concentrations of 10 μM, except for $IZUMO1_{Ig\ domain}$, which was measured at 20 μM. Sedimentation equilibrium analysis was carried out with an XLA-90 analytical centrifuge (Beckman Coulter, Fullerton, CA) in 10 mM Tris-HCl (pH 8.5) and 50 mM NaCl. The isoelectric points of $IZUMO1_{PFF}$ and $IZUMO1_{PFF\text{-}core}$ are 5.4 and 7.8,

respectively. To increase the solubility and avoid unintended aggregation, we carried out all biophysical experiments, including SAXS, at pH 8.5, which is slightly more alkaline than the reported pH of uterine fluid (pH 7.9±0.4) (Iritani et al., 1971). The helix formation of $IZUMO1_{PFF}$ and $IZUMO1_{PFF\text{-}core}$ at neutral pH was confirmed by CD measurements in 10 mM potassium phosphate (pH 7.1) and 150 mM NaCl (supplementary material Fig. S1).

Chemical crosslinking

IZUMO1 fragments (100 μM) were incubated with 25 times molar excess of bis(sulfosuccinimidyl) suberate (BS^3) (Thermo Scientific, Waltham, MA) in 0.1 M HEPES buffer (pH 7.5) at room temperature for 30 minutes, and then the reaction was quenched by 25 mM Tris-HCl (pH 8.5). The samples (1 μg) were subjected to sodium dodecyl sulfate PAGE (SDS-PAGE) under reduced conditions with untreated samples as controls. Mouse spermatozoa from the cauda epididymis were solubilized with phosphate-buffered saline (PBS) with 1% n-dodecyl-β-D-maltoside (DDM) and 1% protease inhibitor cocktail (Nacalai Tesque, Kyoto, Japan). Solubilized proteins were centrifuged at 15,000 ***g*** for 30 minutes at 4°C, and the supernatants were treated with 0.1, 0.5 and 1 mM BS^3 for 2 hours on ice. After incubation, the reaction was stopped with 50 mM Tris-HCl (pH 7.4) for 15 minutes at room temperature. The samples were subjected to non-reducing SDS-PAGE followed by western blotting. IZUMO1 protein was detected with IZUMO1 monoclonal antibody.

SAXS measurement

SAXS measurements were carried out at BL-10C, Photon Factory, Tsukuba, Japan (Ueki et al., 1985). The wavelength of X-rays was 1.488 Å, as selected by a Si monochromator. The scattering profiles were collected using an R-Axis VII (Rigaku, Tokyo, Japan) and the circularly averaged intensity was used for further analysis. The sample cell had a path length of 1 mm. SAXS data were measured at 15°C in 50 mM Tris-HCl (pH 8.5). SAXS data of $IZUMO1_{PFF\text{-}core}$ were collected at the protein concentrations of 12.9, 10.4, 7.9, 5.1 and 2.5 mg/ml. As a control, scattering profiles from lysozyme that was dissolved in the same buffer at the protein concentrations of 15.7, 12.6, 9.5, 6.2 and 3.1 mg/ml were also measured.

Calculation of the pair-distance distribution [*p*(r)] function

The raw data of SAXS measurements were initially analyzed by Igor Pro (WaveMetrics, Lake Oswego, OR) to calculate the scattering intensities from protein by subtracting the intensity curve that was obtained for the buffer solution and to correct for the protein concentration dependency. The scattering curves after these corrections were analyzed to compute $p(r)$ functions using the program GNOM (Svergun, 1992). The analysis was performed by changing the approximate d_{max} value, and the value with which the $p(r)$ function fell to a natural minimum was determined as the real d_{max}. Scattering data in the Q range of 0.02 to 0.24 $Å^{-1}$ were used in this calculation.

Culture cell-adhesion assay

The cloned mouse *Izumo1* cDNA was ligated into the mammalian expression vector pCXN-2 and Cos-7 cells were transiently transfected with this vector using lipofectamine LTX (Life Technologies). After 2 days, transfected Cos-7 cells were collected with 10 mM EDTA-PBS, washed three times with PBS, and suspended in TYH medium. Mouse eggs expressing green fluorescent protein (GFP) in the cytosol were obtained from transgenic mice with an enhanced GFP cDNA under the control of a chicken β-actin promoter and cytomegalovirus enhancer (Okabe et al., 1997). Wild-type and GFP-expressing zona-free oocytes were prepared as above and incubated with transfected Cos-7 cells at 37°C in TYH medium. IZUMO1 was stained by Alexa Fluor 546-fluoresceinated anti-IZUMO1 monoclonal antibodies.

RESULTS

Fusion inhibitory antibodies bound to the N-terminal region of IZUMO1

Our previous report indicated that glycosylation was not essential for IZUMO1 function (Inoue et al., 2008). Therefore, we speculated

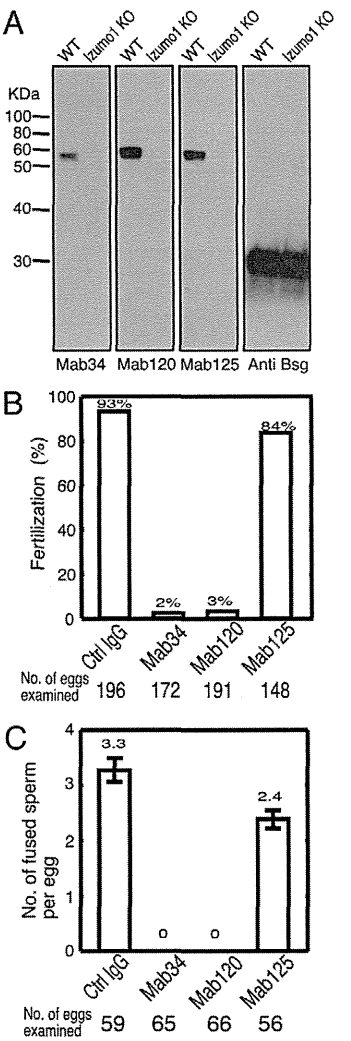

Fig. 2. Establishment of inhibitory monoclonal antibodies to IZUMO1 in sperm-egg fusion *in vitro*. (**A**) All antibodies were immunoreactive against the 56 kDa protein IZUMO1 in wild-type spermatozoa but not in *Izumo1*-null spermatozoa. Solubilized sperm protein (10 μg) was subjected to sodium dodecyl sulfate PAGE (SDS-PAGE), western blotting and detection with anti-IZUMO1 monoclonal antibodies under non-reduced conditions. Basigin (BSG) is shown in the bottom panel as a control. (**B**,**C**) The inhibitory effects of these antibodies were investigated in *in vitro* fertilization and the sperm-egg fusion assay. The *in vitro* fertilization rate was assessed after two-cell development (n=5) (B). Average numbers of fused spermatozoa were observed 30 minutes after insemination (n=3) (C). Total numbers of examined eggs are shown at the bottom of each graph. All analyses were performed in the presence of 10 μg/ml of control IgG, Mab34, Mab120 and Mab125 antibodies. Values are presented as means±s.e.m.

that there must be primary amino acid sequences in IZUMO1 that are important for fusion. We tried to identify the functional site using three new anti-IZUMO1 monoclonal antibodies (Mabs), Mab34, Mab120 and Mab125, which were prepared by immunizing female rats with mouse spermatozoa. In western blot analysis, all of the antibodies detected 56 kDa proteins in wild-type spermatozoa but not in *Izumo1*-null spermatozoa (Fig. 2A), indicating that all of the Mabs are specific for the detection of IZUMO1 in western

blotting. We added these Mabs to an *in vitro* fertilization system and found that only Mab34 and Mab120 significantly inhibited fertilization (Fig. 2B). When the spermatozoa were incubated with zona-free eggs in the presence of these antibodies, the sperm-egg binding was not affected by either of these inhibitory antibodies, but the fusion step was significantly inhibited at a concentration of 10 μg/ml (Mab34 and Mab120) by the sperm-egg fusion assay (Fig. 2C). We measured the concentration dependence of the inhibitory activity of these antibodies, and the inhibition of *in vitro* fertilization was observed even at 0.2 μg/ml of Mab34 and Mab120 (supplementary material Fig. S2).

To search for the functional site of IZUMO1, we separated the sequence of the extracellular region of IZUMO1 into three sections, taking into account the immunoglobulin-like domain. These regions correspond to Asp5-Leu113, Glu146-Leu232 and Pro234-Arg298 (Fig. 1). Of these fragments of IZUMO1, the fusion inhibitory Mabs, Mab34 and Mab120, bound only to the fragment from Asp5 to Leu113, as judged by SPR spectroscopy (Fig. 3A,B). This result indicated that the epitopes of these antibodies are located at the N-terminal region of IZUMO1 (from Asp5 to Leu113) and constitute a putative functional site. We therefore called this fragment 'IZUMO1 putative functional fragment' ($IZUMO1_{PFF}$) (Fig. 1). The dissociation constants of Mab34 and Mab120 were calculated as 1.4 nM (supplementary material Fig. S3A) and 36 nM (supplementary material Fig. S3B), respectively, based on the monomer concentration of $IZUMO1_{PFF}$. Noninhibitory Mab125 recognized $IZUMO1_{234\text{-}298}$, which is a proline-rich juxtamembrane region corresponding to the area between the immunoglobulin-like loop and the transmembrane domain (Fig. 3C). OBF13, which is the original anti-IZUMO1 Mab of the IgM class that was reported to inhibit sperm-egg fusion (Okabe et al., 1987; Inoue et al., 2005), also recognized the $IZUMO1_{PFF}$ fragment, albeit weakly (Fig. 3D).

To further scrutinize the antigenic and biophysical properties of $IZUMO1_{PFF}$, we pursued the identification of the structural core of this fragment. Partially purified $IZUMO1_{PFF}$ was incubated with proteinase K at 10°C for 1.5-2 hours, and a major protease-resistant fragment corresponding to residues Val57-Leu113 was recovered by reverse-phase chromatography, suggesting that this fragment folds into a stable structural core. Therefore, we named this fragment $IZUMO1_{PFF\text{-}core}$ (Fig. 1). In addition to this fragment, an N-terminal region of $IZUMO1_{PFF}$ [named $IZUMO1_{5\text{-}56}$ (Asp5-Ala56)] and a short version of $IZUMO1_{PFF}$ lacking the N-terminal 21 amino acid residues [$IZUMO1_{26\text{-}113}$ (His26-Leu113)] were prepared (Fig. 1). None of these short fragments interacted with Mab34 and Mab120 (supplementary material Fig. S4), suggesting that the antibody recognition depends on the tertiary structure of the antigen.

Egg binding and fusion inhibitory activities of IZUMO1 fragments

Because $IZUMO1_{PFF}$ was a candidate for the functional site of sperm-egg fusion, we asked whether it bound to eggs. We produced Alexa Fluor 546-conjugated $IZUMO1_{PFF}$, $IZUMO1_{PFF\text{-}core}$ and $IZUMO1_{5\text{-}56}$ via an additional C-terminal cysteine by thiol-maleimide coupling. These fluoresceinated fragments were incubated with zona-free unfertilized eggs (Fig. 4A-C). The fragments bound to eggs, and the eggs became fluorescent. The

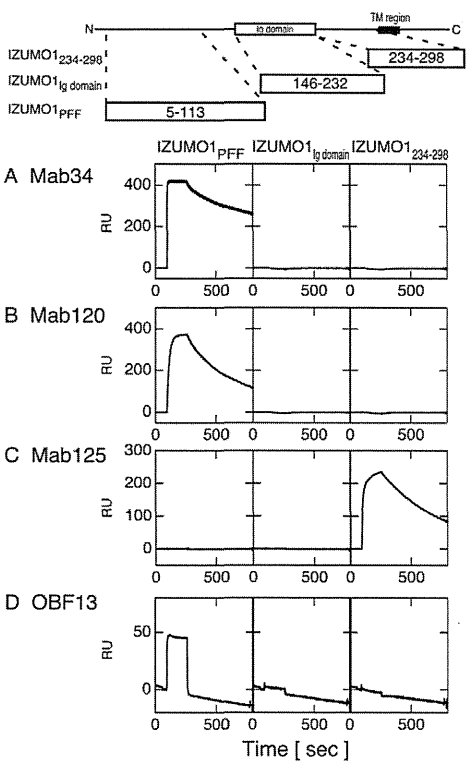

Fig. 3. Interaction of antibodies against the IZUMO1 fragments. (**A-D**) Surface plasmon resonance (SPR) spectra of Mab34 (A), Mab120 (B), Mab125 (C) and OBF13 (D) with 20 μg/ml of $IZUMO1_{PFF}$ (molar concentration is 1.5 μM, assuming the monomer in solution; left panels), $IZUMO1_{Ig\ domain}$ (2.0 μM; middle) and $IZUMO1_{234\text{-}298}$ (2.3 μM; right) were measured.

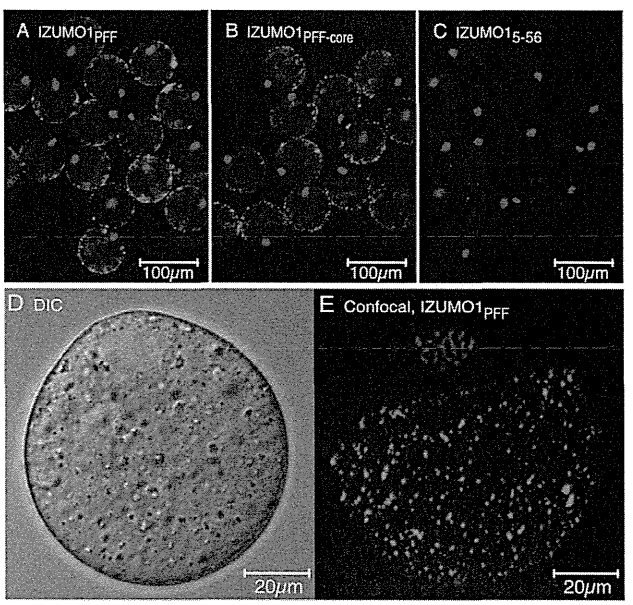

Fig. 4. Binding of IZUMO1 fragments to the egg surface. (**A-C**) The binding of $IZUMO1_{PFF}$ (A), $IZUMO1_{PFF\text{-}core}$ (B) and $IZUMO1_{5\text{-}56}$ (C) to the wild-type egg surface. (**D**,**E**) Differential interference contrast (DIC) (D) and confocal (E) images were taken of the egg with fluoresceinated $IZUMO1_{PFF}$. The egg plasma membrane and nucleus are stained by fluoresceinated IZUMO1 fragments (3 μM) and Hoechst 33342, respectively.

binding of $IZUMO1_{PFF}$ and $IZUMO1_{PFF\text{-}core}$ to eggs was significantly stronger than that of $IZUMO1_{5\text{-}56}$. To investigate precisely the localization of $IZUMO1_{PFF}$ bound on eggs, we acquired differential interference contrast and confocal images of eggs that were incubated with fluoresceinated $IZUMO1_{PFF}$ (Fig. 4D,E). $IZUMO1_{PFF}$ was observed at microvilli-rich regions but not at microvilli-negative regions on the surface of metaphase II chromosomes. The nonuniform distribution of bound $IZUMO1_{PFF}$ suggested that the association between $IZUMO1_{PFF}$ and the egg surface that was observed here was caused by a specific interaction.

Next, we measured sperm-egg fusion in the presence of $IZUMO1_{PFF}$ to ask whether $IZUMO1_{PFF}$ directly affected fertilization (Fig. 5A-C). No significant inhibition was demonstrated by the addition of $IZUMO1_{5\text{-}56}$, $IZUMO1_{PFF\text{-}core}$ and $IZUMO1_{Ig\ domain}$. However, the addition of more than 8 μM $IZUMO1_{PFF}$ significantly inhibited the sperm-egg fusion, and the fusion index (number of spermatozoa that fused to each egg) significantly decreased (Fig. 5C; supplementary material Fig. S5) without affecting sperm motility and egg-binding ability, indicating that the inhibitory effect on fusion occurs during the sperm-egg fusion step and is not based on the sperm-egg binding. These results show that the $IZUMO1_{PFF}$ region is sufficient for both the egg-binding ability and sperm-egg fusion inhibitory activity, and they suggest that this fragment includes the functional site of IZUMO1. In addition, the inhibitory activity of $IZUMO1_{PFF}$ might not come from the saturation of an unknown egg surface receptor for IZUMO1 because $IZUMO1_{PFF\text{-}core}$ bound to eggs but did not prevent the sperm-egg fusion.

$IZUMO1_{PFF}$ bound to the egg surface (Fig. 4) and inhibited sperm-egg fusion *in vitro* (Fig. 5). Therefore, it is plausible that binding partners of IZUMO1 such as CD9 exist on the egg surface. To our surprise, although CD9 is an essential factor for eggs to fuse with spermatozoa, $IZUMO1_{PFF}$ could bind to *Cd9*-null eggs (Fig. 6). Fluoresceinated $IZUMO1_{PFF}$ staining exhibited larger and denser spots than CD9 staining (Fig. 4E) (Inoue et al., 2012). These indicate that there is no physical binding between $IZUMO1_{PFF}$ and

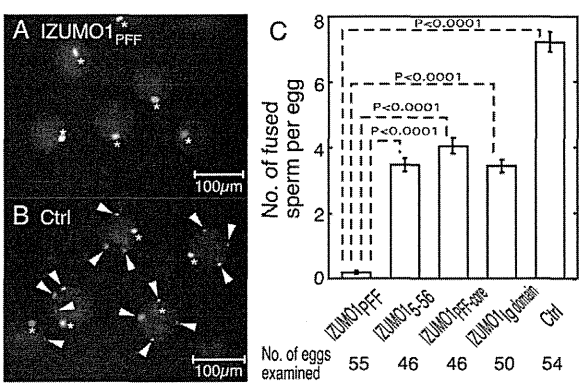

Fig. 5. Effects of IZUMO1 fragments on sperm-egg fusion *in vitro*. (**A**,**B**) The penetration of spermatozoa was examined in the presence of 8 μM $IZUMO1_{PFF}$ (A) and control samples without fragments (B). Fused spermatozoa were stained using Hoechst 33342 that was preloaded into the egg. The arrowheads and asterisks indicate fused spermatozoa and metaphase II-arrested chromosomes, respectively. (**C**) The average number of fused spermatozoa was determined in the presence (8 μM) and absence of fragments. The number of spermatozoa that were fused to an egg was counted using ~50 eggs in each group (n=3). Values are presented as mean±s.e.m.

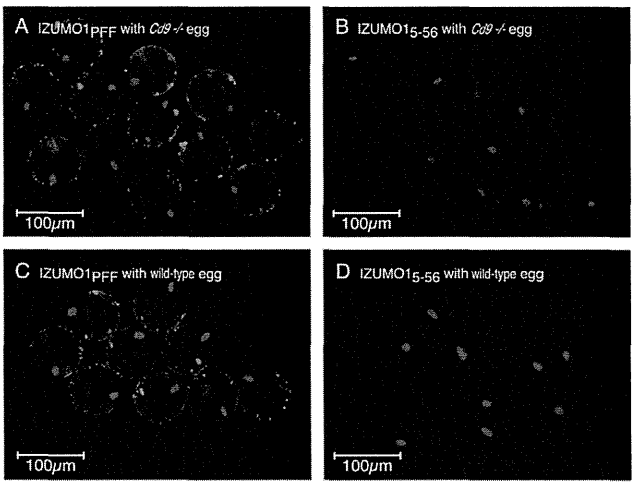

Fig. 6. Interaction of IZUMO1 fragment with $Cd9^{-/-}$ egg surface. (**A-D**) Binding of $IZUMO1_{PFF}$ (A,C) and $IZUMO1_{5\text{-}56}$ (B,D) to the $Cd9^{-/-}$ (A,B) and wild-type (C,D) egg surface. The eggs were stained with 3 μM Alexa Fluor 546-conjugated IZUMO1 fragments.

CD9. The lack of interaction between $IZUMO1_{PFF}$ and CD9 led us to hypothesize the existence of unknown factors that are involved in gamete fusion. Although CD9-related microvillus formation is considered crucial for fusion, our results suggest that the binding of IZUMO1 to the egg surface may not require a CD9-related strong interaction and/or microvillous formation.

An ellipsoidal helix dimer structure as the putative functional site of IZUMO1

A variety of biophysical analyses of protein solution gives us important information about the structure and size of the target molecule. The CD spectroscopy, which monitors the differences between the absorptions of left-handed and right-handed circularly polarized light, is often used to estimate the contents of secondary structures, as well as to examine whether the target protein is denatured, in combination with equilibrium denaturation experiments. A single measurement of a CD spectrum typically can be carried out with less than 25 μg of protein, which is less protein than required by other biophysical methods. The sedimentation equilibrium is one of the most reliable methods with which to determine the molecular weight and, thus, the oligomeric state of proteins in solution. The method is almost free from nonspecific interactions with carriers and effects of charged residues of proteins that often cause ambiguous interpretations of data from other methods such as gel filtration or electrophoresis without SDS or denaturants. By SAXS measurement, we can obtain information about the distance distribution between each pair of X-ray diffractive atoms, such as carbon and nitrogen, in a protein. Using the SAXS data, the size and low-resolution shape of the protein in solution can be calculated. We believe that the molecular information from such biophysical analysis as mentioned above supplements the results from physiological experiments, which will be helpful in understanding the precise mechanism of sperm-egg fusion.

CD and sedimentation equilibrium analysis revealed that $IZUMO1_{PFF}$ forms a helix dimer (Fig. 7). The limited proteolysis of $IZUMO1_{PFF}$ suggested that $IZUMO1_{PFF\text{-}core}$ is a structural core of the

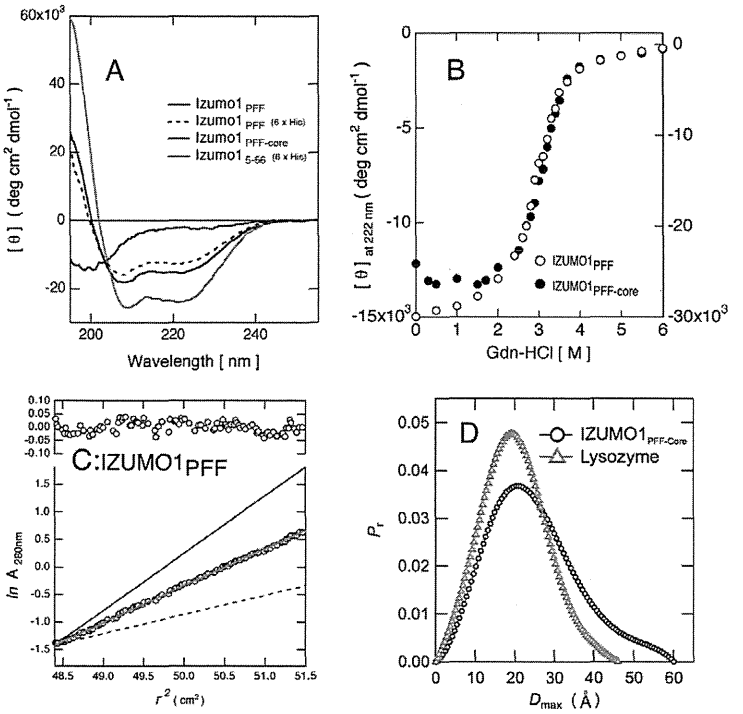

Fig. 7. A series of biophysical measurements of IZUMO1 fragments. (A-D) Circular dichroism (CD) spectra (A), guanidine hydrochloride (GdnHCl)-induced unfolding curves (B), sedimentation equilibrium curves (C) and pair-distance distribution *p(r)* functions (D) of IZUMO1 fragments. (**A**) CD spectra of IZUMO1$_{PFF}$ (black), IZUMO1$_{PFF}$ with His-tag and linker (broken black), IZUMO1$_{PFF\text{-}core}$ (red) and IZUMO1$_{5\text{-}56}$ (blue) were measured For CD measurements, the protein concentration was 10 μM. IZUMO1$_{5\text{-}56}$ has a His-tag and a linker at the C-terminal end. (**B**) The unfolding curves of IZUMO1$_{PFF}$ (open circle) and IZUMO1$_{PFF\text{-}core}$ (closed circle) were detected by ellipticity using a 1 mm cuvette and a protein concentration of 10 μM. The left and right axes are for IZUMO1$_{PFF}$ and IZUMO1$_{PFF\text{-}core}$, respectively. (**C**) Sedimentation equilibrium experiments of IZUMO1$_{PFF}$. The red line is the linear fitting result of the data, indicating that the apparent molecular weight was 25,030. The deviation between the empirical data and the fitted line was plotted in the upper panel. Because the calculated molecular mass of monomeric IZUMO1$_{PFF}$ is 12,916, IZUMO1$_{PFF}$ is predicted to form a dimer. The theoretical lines for a monomer (broken black line) and a trimer (solid black line) are also shown for comparison. The nonlinear fitting analysis gave results that were consistent with those of the linear fitting analysis, in which the differences between these two methods were about 1%. (**D**) *p(r)* functions of IZUMO1$_{PFF\text{-}core}$ (black) and lysozyme (red) were computed by the GNOM program (Svergun, 1992) using their small angle X-ray scattering (SAXS) profiles.

IZUMO1$_{PFF}$ protein. Indeed, IZUMO1$_{PFF\text{-}core}$ exhibited greater negative ellipticity at 222 nm (Fig. 7A). However, the structure of IZUMO1$_{5\text{-}56}$, which is the residual N-terminal region of IZUMO1$_{PFF}$ after IZUMO1$_{PFF\text{-}core}$ is removed, was unfolded, as judged by CD spectroscopy. If the N-terminal region corresponding to IZUMO1$_{5\text{-}56}$ is tightly folded in the context of the whole IZUMO1$_{PFF}$, then IZUMO1$_{PFF}$ should either be more stable than IZUMO1$_{PFF\text{-}core}$ or show a biphasic unfolding transition curve. To examine the stability of both IZUMO1$_{PFF}$ and IZUMO1$_{PFF\text{-}core}$, we tracked ellipticity over a range of GdnHCl-induced unfolding conditions. The midpoint concentrations of unfolding and slopes of transition for both IZUMO1 fragments were identical (Fig. 7B). Combining these data, IZUMO1$_{PFF}$ had a helical structure in its C-terminal region and a mostly unstructured N-terminal region. To assess whether these IZUMO1 fragments formed oligomers, we measured the sedimentation equilibrium profiles at pH 8.5. IZUMO1$_{PFF}$ (Fig. 7C) and IZUMO1$_{PFF\text{-}core}$ (supplementary material Fig. S6A) each exhibited an apparent molecular weight that was 1.9 times its calculated molecular weight, indicating the formation of a dimer in solution, which contrasted with the monomeric characteristic of the IZUMO1$_{Ig\ domain}$ (supplementary material Fig. S6B). The dimerization of IZUMO1$_{PFF}$ and IZUMO1$_{PFF\text{-}core}$ was confirmed by crosslink experiments (supplementary material Fig. S6C). After the reaction of the fragments with the homobifunctional amine-to-amine crosslinker BS^3, we observed decreased monomer fractions and increased dimer fractions by SDS-PAGE of IZUMO1$_{PFF}$ and IZUMO1$_{PFF\text{-}core}$. However, crosslinking is not significant in other fragments. The increased dimeric fraction in the presence of BS^3 was also observed in the intact IZUMO1 in sperm extract (supplementary material Fig. S6D). It is interesting that a small amount of dimeric IZUMO1 can be detected by SDS-PAGE in the absence of BS^3, suggesting that the dimeric structure of intact IZUMO1 is highly stable and that a certain amount of the dimeric form can survive the heat treatment with SDS.

To investigate the molecular shape of IZUMO1$_{PFF\text{-}core}$, we measured the SAXS of both IZUMO1$_{PFF\text{-}core}$ and hen egg white lysozyme as a control because lysozyme has a similar molecular weight to dimeric IZUMO1$_{PFF\text{-}core}$. The *p(r)* function, which is the probable frequency distribution of all vector lengths between atoms within the scattering particle, can provide information about the shape of the protein molecule. The *p(r)* function of IZUMO1$_{PFF\text{-}core}$ showed a larger maximum diameter d_{max} (~60 Å) than that of lysozyme (~46 Å) (Fig. 7D). This difference in d_{max} indicates that the structure of IZUMO1$_{PFF\text{-}core}$ is considerably more elongated than that of a typical globular protein such as lysozyme, suggesting that IZUMO1$_{PFF\text{-}core}$ forms an elongated ellipsoidal shape. The presence of a shoulder in the right side of the *p(r)* function of IZUMO1$_{PFF\text{-}core}$ also supports this idea.

The proline mutant lost egg binding activity and fusion inhibitory activity

Proline is known as a strong helix breaker in aqueous environments (Levitt, 1978). To investigate the functional role of the helix that was identified in the C-terminal region of IZUMO1$_{PFF}$, we prepared a proline mutant of this fragment (IZUMO1$_{PFF\text{-}Pro}$; Fig. 1). As expected, IZUMO1$_{PFF\text{-}Pro}$ lost most of its secondary structure, as shown by CD spectrum (Fig. 8A). The interaction of IZUMO1$_{PFF\text{-}Pro}$ with egg was much weaker than that of IZUMO1$_{PFF}$, but it was similar to that of IZUMO1$_{5\text{-}56}$ (Fig. 8B-D). In addition, no significant fusion inhibitory activity was observed in IZUMO1$_{PFF\text{-}Pro}$ (Fig. 8E). These findings suggested that the helix structure in IZUMO$_{PFF}$ is related to the egg binding and fusion inhibitory effects of IZUMO1$_{PFF}$.

IZUMO1-expressing cultured cells tightly bound egg but did not fuse to egg

To examine whether the IZUMO1 alone can induce the egg binding, which is anticipated from the experiments using IZUMO1$_{PFF}$ and

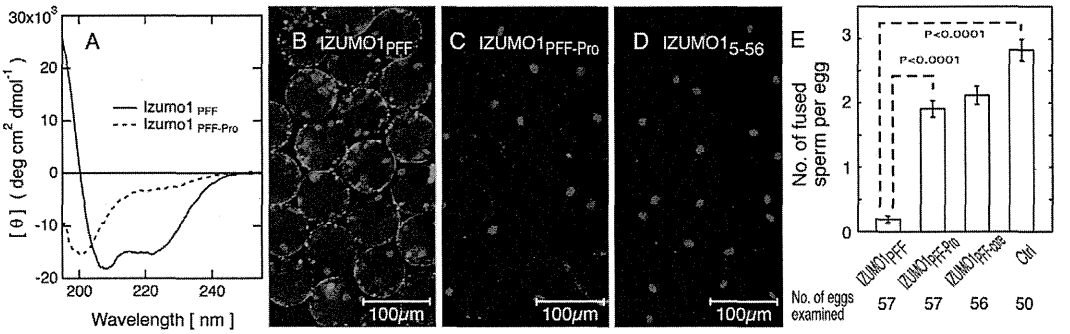

Fig. 8. Influence of helix-breaking mutation on IZUMO1$_{PFF}$. (A-E) Effects of proline mutation on CD spectrum (A), affinity to the egg surface (B-D) and inhibitory activity in sperm-egg fusion *in vitro* (E). (**A**) CD spectra of IZUMO1$_{PFF}$ (black) and IZUMO1$_{PFF-Pro}$ (broken black line) were measured buffer using a 1 mm cuvette and a protein concentration of 10 μM. (**B-D**) The binding of IZUMO1$_{PFF}$ (B), IZUMO1$_{PFF-Pro}$ (C) and IZUMO1$_{5-56}$ (D) to the wild-type egg surface was investigated. The egg plasma membrane and nucleus are stained by fluoresceinated IZUMO1 fragments (3 μM) and Hoechst 33342, respectively. (**E**) The average number of fused spermatozoa in the presence (8 μM) and absence of fragments was calculated. The number of spermatozoa that fused to an egg was counted using ~50 eggs in each group (n=3). Values are presented as mean±s.e.m.

IZUMO1$_{PFF-core}$, we explored the interaction between egg and recombinant Cos-7 cells that were transfected with the expression vector, including mouse intact *Izumo1* cDNA. After 3 hours of incubation of IZUMO1-expressing Cos-7 cells with wild-type eggs, most of the cultured cells were bound to eggs (Fig. 9). This phenomenon was not observed in Cos-7 cells without IZUMO1 expression. In addition, IZUMO1-expressing cells did not aggregate, indicating that the binding of IZUMO1-expressing Cos-7 cells with eggs is a specific interaction that is mediated by IZUMO1. The fusion of two cells, which was judged by the movement of stained nuclei, did not occur even after 24 hour of incubation. We also confirmed that the cytosol fraction of eggs did not disperse within Cos-7 cells after 24 hours of incubation using the eggs that were obtained from transgenic mice expressing GFP. Fluorescence staining by antibody revealed that IZUMO1 accumulated at the interface between Cos-7 and egg cells (Fig. 9B-D). In addition, Cos-7 cells that were bound to eggs were deformed along the egg surface.

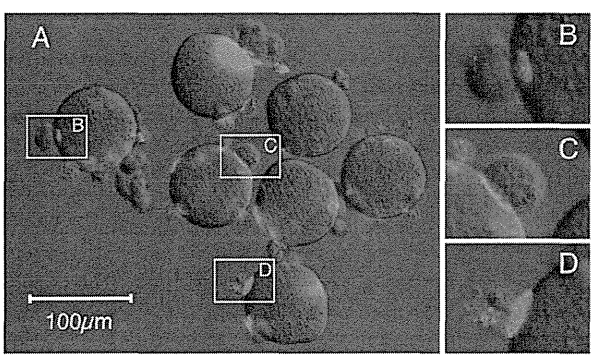

Fig. 9. Interactions between egg and cultured cells transfected with *Izumo1* cDNA. (**A**) Mouse wild-type eggs and Cos-7 cells that were transfected with mouse *Izumo1* cDNA were incubated for 3 hours at 37°C. The fluorescent signal from anti-IZUMO1 monoclonal antibodies that were conjugated with Alexa Fluor 546 was shown in red on the bright-field image. (**B-D**) Magnified image (2.5×) of the region surrounded by the white square in A.

DISCUSSION

In this paper, we have determined that a putative functional site exists in the N-terminal region of IZUMO1. The latter half of this region is important for the binding of IZUMO1 to the egg surface because the fragment corresponding to this part, IZUMO1$_{PFF-core}$, bound to the egg surface. Although CD9 is an essential factor for sperm-egg fusion in eggs, IZUMO1$_{PFF}$ maintains the binding ability on the egg surface of *Cd9*$^{-/-}$ eggs, indicating that the presence of unknown factors that are related to the gamete fusion. A series of CD, sedimentation equilibrium and SAXS experiments showed that IZUMO1$_{PFF}$ was composed of an N-terminal unfolded region and a C-terminal helix dimer with an ellipsoidal shape. In addition, the IZUMO1$_{PFF}$ mutant, IZUMO1$_{PFF-Pro}$, which has a defective helical formation, lost egg-binding and fusion inhibitory activities. These results suggest that the formation of a helical dimer at the N-terminal region is essential for the function of IZUMO1.

Recombinant Cos-7 cells expressing whole IZUMO1 did not fuse to eggs. However, we found that these cultured cells bound to eggs and that IZUMO1 accumulated at the interaction site of the two cells. These observations suggest that IZUMO1 alone cannot cause sperm-egg membrane fusion; rather, it induces cellular surface interactions such as membrane tethering. We speculate that the distance between membranes of the spermatozoon and the egg may be not short enough to trigger membrane fusion when IZUMO1$_{PFF}$ binds to the egg surface. Instead, the helical region of IZUMO1 corresponding to IZUMO1$_{PFF-core}$ may keep the membranes close together. The separation of IZUMO1$_{PFF-core}$ from the transmembrane region by an immunoglobulin-like domain does not contradict the above notion. There are two examples of essential proteins for fusion, which are supposed to tether membranes. Mitofusin is essential for mitochondrial fusion and forms trans complexes between mitochondria. Mfn1, mammalian mitofusin, forms an antiparallel helix dimer. Because the arrangement of helices is antiparallel and the linker between transmembrane and helical regions is relatively long (>40 amino acids), two membranes that are connected by dimeric mitofusin are distant from each other. Thus, Mfn1 is thought to tether mitochondrial membranes during fusion (Koshiba et al., 2004; Detmer and Chan, 2007). EEA1 is essential for early endosome fusion, and it is proposed to tether endosomes by binding phosphatidylinositol at its C terminus and Rab5 at its N terminus (Christoforidis et al., 1999). The crystal

structure of a C-terminal fragment of EEA1 indicates that a parallel helix bundle is formed next to the phosphatidylinositol-binding FYVE domain. The presence of a strong heptad repeat throughout the sequence suggests that EEA1 forms long, continuous coiled coils and holds two membranes together at a significant distance (Dumas et al., 2001). It should be noted that possible membrane interactions that are induced by IZUMO1 should be different from the binding of spermatozoa around eggs because *Izumo1*-deficient spermatozoa seem to have normal attachments to eggs, but this binding may not facilitate sperm-egg fusion (Inoue et al., 2005). CD9 is also suggested to be involved in membrane adhesion to trigger sperm-egg fusion (Jégou et al., 2011), although spermatozoa bound to *Cd9*-null eggs (Miyado et al., 2000).

Chen and Olson referred to IZUMO1 as a typical non-helix protein that was involved in biological membrane fusion because only the immunoglobulin-like domain can be predicted from the primary sequence as a known structural motif (Chen and Olson, 2005). The β-sheet-rich C2 domain is proposed to induce membrane curvature and to be involved directly in the fusion step (Martens and McMahon, 2008). Because of the similarity between the immunoglobulin-like domain and the C2 domain, fusion-related proteins with immunoglobulin-like domains, including IZUMO1, were hypothesized to work in a similar manner to proteins containing C2 domains, such as synaptotagmin. Our finding requires reconsidering such a view about IZUMO1 and also encourages a search for helix motifs in other proteins that are related to cell-cell membrane fusions, such as myoblast formation, multinucleation of macrophages and epithelial fusion in *Caenorhabditis elegans* (Podbilewicz et al., 2006; Sapir et al., 2007; Helming and Gordon, 2009; Abmayr and Pavlath, 2012).

IZUMO1, IZUMO2, IZUMO3 and IZUMO4 share a novel sequence motif called the Izumo domain, which is characterized by the presence of a conserved cluster of eight cysteines: C-X(2)-C-X(106,108)-C-X(3,4)-C-X(9)-C-X(2)-C-X(6)-C-X(4,5)-C (Ellerman et al., 2009). IZUMO1$_{PFF}$ corresponds to the region between the second and third cysteines. The sequence similarity between IZUMO1 and IZUMO2, IZUMO3 and IZUMO4 is not obvious at this region, where the CLUSTAL W scores were 12.2-15.7 (Thompson et al., 1994). Ellerman et al. observed the dimeric form, in addition to monomeric and trimeric forms, of the Izumo domain of IZUMO1 by SDS-PAGE with mildly denaturing conditions. This is consistent with the data that are presented here. However, they could observe neither the binding of recombinant IZUMO1 fragments, which included the Izumo domain, to the egg nor the inhibitory activity of IZUMO1 fragments on sperm-egg fusion *in vitro*. The discrepancy between our data and those of Ellerman et al. could be explained by the presence of cysteine clusters close to the IZUMO1$_{PFF}$ sequences. These cysteines may affect the structure and negatively regulate the function of IZUMO1. Another possibility is that the cysteines prohibit the correct folding of their recombinant fragments by the aberrant formation of disulfide bonds. Recombinant fragments with those cysteines that were expressed in *E. coli* had intermolecular disulfide bonds under oxidized conditions and thus formed oligomers and aggregates (supplementary material Fig. S7). Although the functional and structural roles of the cysteine cluster are unclear, the IZUMO1$_{PFF}$ fragment was mono-dispersed in solution, had a significant amount of secondary structure, was unfolded cooperatively by a denaturant, exhibited egg-binding activity and inhibited sperm-egg fusion. Furthermore, inhibitory antibodies, which were obtained by the immunization of mouse spermatozoa, recognized the tertiary structure of IZUMO1$_{PFF}$, indicating that our recombinant IZUMO1$_{PFF}$ shares the structure of native IZUMO1. These results strongly suggested the correct and functional folding of our fragment. To uncover the physiological functions of the novel IZUMOs, it will be interesting to study the egg-binding and fusion inhibition activities and structural analysis of fragments of IZUMO2, IZUMO3 and IZUMO4 that correspond to IZUMO1$_{PFF}$.

IZUMO1$_{PFF\text{-}core}$ formed an ellipsoidal dimer, and its helical structure is required for the fusion inhibition and egg-binding activities of this fragment. These features are reminiscent of the known fusion-related proteins such as class 1 viral envelope proteins, SNAREs, mitofusin and EEA1, which consist of a bundle of coiled-coil structures. However, we could not identify an unequivocal coiled-coil region by the prediction programs MultiCoil, LearnCoil and Paircoil2 (Wolf et al., 1997; Singh et al., 1999; McDonnell et al., 2006). The mean residue ellipticity at 222 nm of IZUMO1$_{PFF\text{-}core}$ is larger than the ellipticity that is expected in a typical coiled-coil region (O'Shea et al., 1989), but it is similar to that of the SNARE complex (Fasshauer et al., 1997; Rice et al., 1997). It is fascinating that the machinery in sperm-egg fusion may share the structural motif of a helix bundle with other biological viral and vesicle fusions. A high-resolution structural analysis is required to confirm this hypothesis. We found that IZUMO1 fragments can be crystallized with polyethylene glycol as a precipitant; however, the quality of X-ray diffractions of these crystals was not sufficient to solve the three-dimensional structure. We believe that co-crystallization with an antibody fragment may help improve crystal packing (Koide, 2009).

A function-inhibiting and egg-binding IZUMO1$_{PFF}$, which was identified in this report, will be useful in the search for other components of the egg-fusion machinery. Identifying the essential components of the fusion machinery will greatly assist in the elucidation of the sperm-egg fusion mechanism.

Acknowledgements

We are very grateful to Dr Chris C. Liu at University of Toronto and Dr Adam M. Benham at Durham University for critically analyzing the manuscript and providing valuable advice. We thank Dr Eisuke Mekada and Mr Takao Nishikawa at Osaka University for kindly giving us the *Cd9* disrupted mouse line and for technical assistance, respectively. We also thank Professor Amy E. Keating at Massachusetts Institute of Technology and Professor David C. Chan at California Institute of Technology for their helpful comments on the manuscript.

Funding

This work was supported by grants [19570159 to N.I., K.H., M.Y., Y.H.; 21112006 to N.I.; 21687018 to N.I.] and the Global COE Program A08 from the Ministry of Education, Culture, Sports, Science, and Technology of Japan.

Competing interests statement

The authors declare no competing financial interests.

Author contributions

N.I., M.O. and Y.H. designed research; N.I. performed the experiments using sperm and egg; D.H., H.K. and M.K. performed SAXS studies; M.I. generated antibodies; Y.H. performed the biophysical experiments; K.H. and M.Y. performed structural analysis and crystallographic experiments; N.I., M.O. and Y.H. wrote the manuscript.

Supplementary material

Supplementary material available online at
http://dev.biologists.org/lookup/suppl/doi:10.1242/dev.094854/-/DC1

References

Abmayr, S. M. and Pavlath, G. K. (2012). Myoblast fusion: lessons from flies and mice. *Development* **139**, 641-656.

Chen, E. H. and Olson, E. N. (2005). Unveiling the mechanisms of cell-cell fusion. *Science* **308**, 369-373.

Christoforidis, S., McBride, H. M., Burgoyne, R. D. and Zerial, M. (1999). The Rab5 effector EEA1 is a core component of endosome docking. *Nature* **397**, 621-625.
Detmer, S. A. and Chan, D. C. (2007). Functions and dysfunctions of mitochondrial dynamics. *Nat. Rev. Mol. Cell Biol.* **8**, 870-879.
Doering, D. S. and Matsudaira, P. (1996). Cysteine scanning mutagenesis at 40 of 76 positions in villin headpiece maps the F-actin binding site and structural features of the domain. *Biochemistry* **35**, 12677-12685.
Dumas, J. J., Merithew, E., Sudharshan, E., Rajamani, D., Hayes, S., Lawe, D., Corvera, S. and Lambright, D. G. (2001). Multivalent endosome targeting by homodimeric EEA1. *Mol. Cell* **8**, 947-958.
Edelhoch, H. (1967). Spectroscopic determination of tryptophan and tyrosine in proteins. *Biochemistry* **6**, 1948-1954.
Ellerman, D. A., Pei, J., Gupta, S., Snell, W. J., Myles, D. and Primakoff, P. (2009). Izumo is part of a multiprotein family whose members form large complexes on mammalian sperm. *Mol. Reprod. Dev.* **76**, 1188-1199.
Fasshauer, D., Bruns, D., Shen, B., Jahn, R. and Brünger, A. T. (1997). A structural change occurs upon binding of syntaxin to SNAP-25. *J. Biol. Chem.* **272**, 4582-4590.
Helming, L. and Gordon, S. (2009). Molecular mediators of macrophage fusion. *Trends Cell Biol.* **19**, 514-522.
Inoue, N., Ikawa, M., Isotani, A. and Okabe, M. (2005). The immunoglobulin superfamily protein Izumo is required for sperm to fuse with eggs. *Nature* **434**, 234-238.
Inoue, N., Ikawa, M. and Okabe, M. (2008). Putative sperm fusion protein IZUMO and the role of N-glycosylation. *Biochem. Biophys. Res. Commun.* **377**, 910-914.
Inoue, N., Nishikawa, T., Ikawa, M. and Okabe, M. (2012). Tetraspanin-interacting protein IGSF8 is dispensable for mouse fertility. *Fertil. Steril.* **98**, 465-470.
Iritani, A., Nishikawa, Y., Gomes, W. R. and VanDemark, N. L. (1971). Secretion rates and chemical composition of oviduct and uterine fluids in rabbits. *J. Anim. Sci.* **33**, 829-835.
Jégou, A., Ziyyat, A., Barraud-Lange, V., Perez, E., Wolf, J. P., Pincet, F. and Gourier, C. (2011). CD9 tetraspanin generates fusion competent sites on the egg membrane for mammalian fertilization. *Proc. Natl. Acad. Sci. USA* **108**, 10946-10951.
Kaji, K., Oda, S., Shikano, T., Ohnuki, T., Uematsu, Y., Sakagami, J., Tada, N., Miyazaki, S. and Kudo, A. (2000). The gamete fusion process is defective in eggs of Cd9-deficient mice. *Nat. Genet.* **24**, 279-282.
Koide, S. (2009). Engineering of recombinant crystallization chaperones. *Curr. Opin. Struct. Biol.* **19**, 449-457.
Koshiba, T., Detmer, S. A., Kaiser, J. T., Chen, H., McCaffery, J. M. and Chan, D. C. (2004). Structural basis of mitochondrial tethering by mitofusin complexes. *Science* **305**, 858-862.
Le Naour, F., Rubinstein, E., Jasmin, C., Prenant, M. and Boucheix, C. (2000). Severely reduced female fertility in CD9-deficient mice. *Science* **287**, 319-321.
Letunic, I., Copley, R. R., Pils, B., Pinkert, S., Schultz, J. and Bork, P. (2006). SMART 5: domains in the context of genomes and networks. *Nucleic Acids Res.* **34** Database issue, D257-D260.
Levitt, M. (1978). Conformational preferences of amino acids in globular proteins. *Biochemistry* **17**, 4277-4285.
Martens, S. and McMahon, H. T. (2008). Mechanisms of membrane fusion: disparate players and common principles. *Nat. Rev. Mol. Cell Biol.* **9**, 543-556.
McDonnell, A. V., Jiang, T., Keating, A. E. and Berger, B. (2006). Paircoil2: improved prediction of coiled coils from sequence. *Bioinformatics* **22**, 356-358.
McGuffin, L. J. and Jones, D. T. (2003). Improvement of the GenTHREADER method for genomic fold recognition. *Bioinformatics* **19**, 874-881.
Miyado, K., Yamada, G., Yamada, S., Hasuwa, H., Nakamura, Y., Ryu, F., Suzuki, K., Kosai, K., Inoue, K., Ogura, A. et al. (2000). Requirement of CD9 on the egg plasma membrane for fertilization. *Science* **287**, 321-324.
O'Shea, E. K., Rutkowski, R. and Kim, P. S. (1989). Evidence that the leucine zipper is a coiled coil. *Science* **243**, 538-542.
Okabe, M., Adachi, T., Takada, K., Oda, H., Yagasaki, M., Kohama, Y. and Mimura, T. (1987). Capacitation-related changes in antigen distribution on mouse sperm heads and its relation to fertilization rate in vitro. *J. Reprod. Immunol.* **11**, 91-100.
Okabe, M., Ikawa, M., Kominami, K., Nakanishi, T. and Nishimune, Y. (1997). 'Green mice' as a source of ubiquitous green cells. *FEBS Lett.* **407**, 313-319.
Podbilewicz, B., Leikina, E., Sapir, A., Valansi, C., Suissa, M., Shemer, G. and Chernomordik, L. V. (2006). The C. elegans developmental fusogen EFF-1 mediates homotypic fusion in heterologous cells and in vivo. *Dev. Cell* **11**, 471-481.
Primakoff, P. and Myles, D. G. (2007). Cell-cell membrane fusion during mammalian fertilization. *FEBS Lett.* **581**, 2174-2180.
Rice, L. M., Brennwald, P. and Brünger, A. T. (1997). Formation of a yeast SNARE complex is accompanied by significant structural changes. *FEBS Lett.* **415**, 49-55.
Sapir, A., Choi, J., Leikina, E., Avinoam, O., Valansi, C., Chernomordik, L. V., Newman, A. P. and Podbilewicz, B. (2007). AFF-1, a FOS-1-regulated fusogen, mediates fusion of the anchor cell in C. elegans. *Dev. Cell* **12**, 683-698.
Singh, M., Berger, B. and Kim, P. S. (1999). LearnCoil-VMF: computational evidence for coiled-coil-like motifs in many viral membrane-fusion proteins. *J. Mol. Biol.* **290**, 1031-1041.
Svergun, D. I. (1992). Determination of the regularization parameter in indirect-transform methods using perceptual criteria. *J. Appl. Cryst.* **25**, 495-503.
Thompson, J. D., Higgins, D. G. and Gibson, T. J. (1994). CLUSTAL W: improving the sensitivity of progressive multiple sequence alignment through sequence weighting, position-specific gap penalties and weight matrix choice. *Nucleic Acids Res.* **22**, 4673-4680.
Ueki, T., Hiragi, Y., Kataoka, M., Inoko, Y., Amemiya, Y., Izumi, Y., Tagawa, H. and Muroga, Y. (1985). Aggregation of bovine serum albumin upon cleavage of its disulfide bonds, studied by the time-resolved small-angle X-ray scattering technique with synchrotron radiation. *Biophys. Chem.* **23**, 115-124.
Wolf, E., Kim, P. S. and Berger, B. (1997). MultiCoil: a program for predicting two- and three-stranded coiled coils. *Protein Sci.* **6**, 1179-1189.
Yamagata, K., Nakanishi, T., Ikawa, M., Yamaguchi, R., Moss, S. B. and Okabe, M. (2002). Sperm from the calmegin-deficient mouse have normal abilities for binding and fusion to the egg plasma membrane. *Dev. Biol.* **250**, 348-357.
Zdobnov, E. M. and Apweiler, R. (2001). InterProScan—an integration platform for the signature-recognition methods in InterPro. *Bioinformatics* **17**, 847-848.

Sciencexpress Reports

Structural Basis for the Counter-Transport Mechanism of a H^+/Ca^{2+} Exchanger

Tomohiro Nishizawa,[1,5] Satomi Kita,[2] Andrés D. Maturana,[3] Noritaka Furuya,[1] Kunio Hirata,[4] Go Kasuya,[1] Satoshi Ogasawara,[5] Naoshi Dohmae,[6] Takahiro Iwamoto,[2] Ryuichiro Ishitani,[1,6*] Osamu Nureki[1,6*]

[1]Department of Biophysics and Biochemistry, Graduate School of Science, The University of Tokyo, 2-11-16 Yayoi, Bunkyo-ku, Tokyo 113-0032, Japan. [2]Department of Pharmacology, Faculty of Medicine, Fukuoka University, 7-45-1 Nanakuma, Jonan-ku, Fukuoka 814-0180, Japan. [3]Department of Bioengineering Sciences, Graduate School of Bioagricultural Sciences, Furo-cho, Chikusa-ku, Nagoya 464-8601, Nagoya University, Japan. [4]RIKEN SPring-8 Center, Hyogo 679-5148, Japan. [5]Graduate School of Medicine and Faculty of Medicine, Kyoto University, Konoe-cho Yoshida Sakyo-ku Kyoto 606-8501, Japan. [6]RIKEN Advanced Science Institute, 2-1 Hirosawa, Wako-shi, Saitama 351-0198, Japan.

*Corresponding author. E-mail: nureki@biochem.s.u-tokyo.ac.jp (O.N.); ishitani@biochem.s.u-tokyo.ac.jp (R.I.)

Ca^{2+}/cation antiporters catalyze the exchange of Ca^{2+} with various cations across biological membranes, to regulate cytosolic calcium levels. The recently reported structure of a prokaryotic Na^+/Ca^{2+} exchanger (NCX_Mj) revealed its overall architecture in an outward-facing state. Here we report the crystal structure of a H^+/Ca^{2+} exchanger from *Archaeoglobus fulgidus* (CAX_Af) in the two representatives of the inward-facing conformation at 2.3 Å resolution. The structures suggested Ca^{2+} or H^+ binds to the cation-binding site mutually exclusively. Structural comparison of CAX_Af with NCX_Mj revealed that the first and sixth transmembrane helices alternately create hydrophilic cavities on the intra- and extracellular sides. The structures and functional analyses provide insight into the mechanism of how the inward- to outward-facing state transition is triggered by the Ca^{2+} and H^+ binding.

Calcium ions are involved in diverse physiological processes, such as muscle contraction, cell proliferation, exocytosis, and apotosis (*1–3*). The Ca^{2+}/cation antiporter (CaCA) superfamily members are important regulators of cytosolic Ca^{2+} levels (*4–6*). They use the electrochemical gradient of other cations, such as Na^+, H^+, or K^+, to catalyze Ca^{2+} transport across biological membranes (*4–6*). The CaCA superfamily comprises five major groups: Na^+/Ca^{2+} exchangers (NCX), K^+-dependent Na^+/Ca^{2+} exchangers (NCKX), H^+/Ca^{2+} exchangers (CAX), cation/Ca^{2+} (other cation than Na^+, H^+, or K^+) exchangers (CCX), and bacterial homologous gene (YrbG) (*6*, *7*). All CaCA proteins contain two highly conserved α-repeat regions (α-1 and α-2), which are thought to have arisen from an ancient gene duplication event (*6*, *8*), and are reportedly important for cation binding and transport (*8–10*).

Recently, the crystal structure of the Na^+/Ca^{2+} exchanger from *Methanococcus jannaschii* (NCX_Mj) in an outward-facing state was reported, revealing a pseudo-symmetric architecture formed by two structural repeats of 5 transmembrane (TM) helices with opposite orientations (*10*). Three Na^+ sites and one Ca^{2+}-specific site were observed within the cation binding pocket, leading to an exchange model in which the sequential binding of three Na^+ ions causes the release of Ca^{2+} during the exchange cycle (*10*). However, the mechanism by which Ca^{2+} and the counter-transported cations stimulate the structural transition between the inward- and outward-facing states remains elusive (*4*, *5*, *11*), because of the lack of the structural information of its inward-facing state. Furthermore, the molecular basis for the cation recognition in other members of the CaCA superfamily remains unclear.

We performed the structural analysis of a CaCA homolog from *Archaeoglobus fulgidus* (CAX_Af). Liposome- and *E. coli*-based transport assays confirmed that the homolog has H^+/Ca^{2+} exchange activity (Fig. 1A and figs. S1, S2, and S3). The purified CAX_Af protein was crystallized by the lipidic cubic phase (LCP) method (*12*) under low pH (6.0-6.5) conditions. The structure was determined by the multiple anomalous diffraction method using mercury derivatives, and refined to 2.3 Å resolution (table S1). The crystallographic asymmetric unit contained two molecules (Mol A and Mol B) (fig. S4). Since the overall architectures of these two molecules were essentially identical (root mean square deviation of 1.04 Å over all Cα atoms), we focus on the Mol A structure.

The structure of CAX_Af contains 12 TM helices, with both N and C ends located on the intracellular side (Fig. 1, B to D). The core domain (TM2-5 and TM7-10) is tightly packed together, while the gating bundle, consisting of the long TM1 and TM6 helices, is loosely packed against the core domain (Fig. 1, C and D). The core domain shares structural similarity with NCX_Mj (*10*); their N and C terminal halves (TM2-5 and TM7-10, respectively) are related by a pseudo two-fold rotational axis within the molecule. The two conserved α-repeats (*6*) consist of TM2 and TM3 for α-1 and TM7 and TM8 for α-2 (figs. S5 and S6). CAX_Af contains two additional TM helices (N- and C-helices) (Fig. 1, B to D). These helices are not conserved throughout the CaCA family (*6*), suggesting that they are not involved in the common exchange mechanism.

While the structure of the core domain of CAX_Af is almost identical to that of NCX_Mj, the conformation of the gating bundle is different (Fig. 2, A and B). The structure of NCX_Mj represents an outward-facing conformation, with its ion binding sites accessible from the extracellular side through an outward-facing cavity (Fig. 2A). TM6 of the gating bundle adopts a straight conformation, which forms the outward-facing cavity with the extracellular halves of TM2 and TM7 (Fig. 2A). TM1 of the gating bundle adopts a bent conformation, and is tightly packed against the intracellular halves of TM2 and TM7 (Fig. 2A). Consequently, the ion binding sites are completely occluded from the intracellular space (*10*). Relative to the NCX_Mj structure, the conformation of the gating bundle of CAX_Af is symmetrically inverted (Fig. 2B). TM6 of the gating bundle adopts a bent conformation and is closely packed against the extracellular halves of TM2 and TM7, with hydrophobic interactions through Phe^{227}, Leu^{231}, and Leu^{232} in TM6 (Fig. 2C). TM1 of the gating bundle adopts a straight conformation, creating a cavity surrounded by the intracellular halves of TM1, TM2, TM7, and TM8 (Fig. 2D). Therefore, the present structure of CAX_Af represents an inward-facing conformation.

A comparison between the inward-facing CAX_Af and outward-facing

NCX_Mj suggested that the structural changes of the gating bundle (TM1 and TM6) alternately create hydrophilic cavities suitable for cation permeation on the intra- and extracellular sides. In both CAX_Af and NCX_Mj structures, the intracellular half of TM1 and the extracellular half of TM6 are amphipathic. In the inward-facing structure of CAX_Af, a hydrophilic cluster on the TM1 helix ($Ser4^{7}$, Ser^{51}, Glu^{55}, and Glu^{58}) faces toward the inward-facing cavity (Fig. 2D), rendering the cavity hydrophilic, while a hydrophilic cluster on the extracellular side of the TM6 helix (Glu^{225}, Glu^{229}, and Glu^{233}) faces away from the core domain (Fig. 2C). In contrast, in the outward-facing structure of NCX_Mj, the hydrophilic cluster on TM6 faces toward the core domain, thereby forming the hydrophilic outward-facing cavity (Fig. 2A). The transition to the outward-facing state may involve a sliding motion of the gating bundle that brings the extracellular hydrophilic cluster of TM1 to the outward-facing cavity, while its hydrophobic side seals the inward-facing cavity (Movie S1). The second ion passageway in the NCX_Mj structure, which was suggested to be involved in the Na^+ permeation (*10*), does not exist in the CAX_Af structure. These hydrophilic clusters on the gating bundle are conserved among other CaCA proteins as well (fig. S5), suggesting that this alternate formation of the hydrophilic cavities is a common mechanism in the CaCA superfamily.

The Ca^{2+} binding site of NCX_Mj is formed by Glu and Pro residues (Pro^{53}, Glu^{54}, Pro^{212}, and Glu^{213}), which constitute the signature motifs in the α-repeat sequence (Fig. 3A and fig. S5) (*6*, *10*). The side chain carboxylates of Glu^{54} and Glu^{213} coordinate the bound Ca^{2+} in a bidentate fashion (Fig. 3A). TM2 and TM7 are kinked at Pro^{53} and Pro^{212}, facilitating further coordination of Ca^{2+} by the backbone carbonyls of Thr^{50} and Thr^{209} (Fig. 3A) (*10*). In CAX_Af, the Pro and Glu residues of the signature motif are also conserved (Pro^{77}, Glu^{78}, Pro^{257}, and Glu^{258}), with TM2 and TM7 kinked at Pro^{77} and Pro257 (Fig. 3B and fig. S6). The backbone carbonyls of Ala^{74} and Ser^{254} located at these kinks protrude into the space between TM2 and TM7, to coordinate a water molecule together with Ser^{47}, and Glu^{78} and Glu^{258} are situated at similar positions to their counterparts in NCX_Mj. This structural similarity suggests that these conserved residues of CAX_Af are also involved in Ca^{2+} binding (Fig. 3B). However, in the structure of CAX_Af, we observed no electron density peak corresponding to Ca^{2+} (fig. S7), and the side chain carboxylate groups of Glu^{78} and Glu^{258} were oriented in different directions (Fig. 3B). Instead of the Ca^{2+} coordination, Glu^{78} forms a hydrogen bond network with the side chains of Asn^{103} and Ser^{254}, and the backbone carbonyl of Val^{246}, located on the extracellular half of the membrane (H_{ext}; Fig. 3B). The hydrogen bonding patterns and geometries of H_{ext} suggested that the side chain carboxylate of Glu^{78} is protonated (Fig. 3D). In the middle of the membrane, Glu^{258} forms another hydrogen bond network with the side chains of Glu^{255}, Ser^{281}, and Gln^{285} (H_{mid}) (Fig. 3, B and E). Mutation of Glu^{255} or Gln^{285} to alanine significantly decreased the pH-dependent Ca^{2+} uptake in liposomes (Fig. 3H and fig. S9), indicating the importance of the H_{mid} network for the H^+/Ca^{2+} exchange activity. Within the H_{mid} network, the hydrogen bonding patterns and geometries also suggested that the side chain carboxylates of Glu^{255} and Glu^{258} are protonated (Fig. 3E). The protonation state assignments of Glu^{78}, Glu^{255}, and Glu^{258} are consistent with the fact that these residues are embedded in the low dielectric environment of the TM segments, and that the crystal was obtained under low-pH conditions (pH 6.0–6.5). The Ala or Gln mutation of either Glu^{78}, Glu^{255}, or Glu^{258} decreased the H^+/Ca^{2+} exchange activity (Fig. 3H), indicating the importance of their protonation and deprotonation during the exchange cycle. The residues involved in the H_{ext} and H_{mid} networks (Ser^{254}, Glu^{255}, Ser^{281}, and Gln^{285}) are located at equivalent positions to the Na^+ coordinating residues in NCX_Mj (Fig. 3, A and B, and fig. S5). Taken together, the structural comparison with NCX_Mj suggests that the space formed between the kinks of TM2 and TM7 is the Ca^{2+} binding site (S_{Ca}) (Fig. 3B), whereas the hydrogen bonding networks (H_{mid} and H_{ext}) (Fig. 3B) involving Glu^{78}, Glu^{255}, and Glu^{258} can function as the H^+ binding sites.

The Glu^{78} and Glu^{258} residues are involved in both Ca^{2+} and H^+ binding, further suggesting that the binding of Ca^{2+} and H^+ to these sites is mutually exclusive, which is consistent with the counter-transporting mechanism of the CaCA superfamily (*4*). The present crystal structure presumably represents the H^+ bound state, and thus cannot accommodate Ca^{2+}. Supporting this notion, Ca^{2+} is not bound to S_{Ca}, even though the crystal was obtained in the presence of 10 mM $CaCl_2$ (fig. S7).

As described above, the crystallographic asymmetric unit contains two molecules of CAX_Af (Mol A and Mol B). The Mol B structure exhibited different hydrogen bonding patterns in the H_{mid} network. In Mol B, the carboxylate group of Glu^{258} does not form hydrogen bonds with Ser^{281} and Glu^{255}, and is exposed toward the inward-facing cavity (Fig. 3C), suggesting that Glu^{258} is deprotonated (Fig. 3G and fig. S8). As a result, H_{mid} is partially disrupted in Mol B (Fig. 3, C and G). In Mol A, the hydrogen bond interactions in H_{mid} bridge TM7 and TM8, stabilizing the arrangement of TM7 in the core domain (Fig. 3, B and E). In contrast, in Mol B, the fewer hydrogen bonds in H_{mid} resulted in the slight twisting of TM7 as compared with that in Mol A (Fig. 3C and fig. S10), allowing the accommodation of a monoolein acyl chain in the inward-facing cavity. This twisting of TM7 changes the directions of its side chains; Pro^{257} is shifted toward the gating bundle (fig. S10). Consequently, there is a large gap between Pro^{77} (TM2) and Pro^{257} (TM7) in Mol B (Fig. 4B). Altogether, these observations suggested that Mol B represents a "partially" protonated state, while Mol A represents the "fully" protonated state after binding H^+. The protonation of Glu^{258} in H_{mid} tighten the interaction between TM7 and TM8, which results in the twisting of TM7 toward the H^+/Ca^{2+} binding pocket to close the gap between Pro^{77} and Pro^{257} (Fig. 4, A and B, and fig. S10).

In the structure of NCX_Mj, Pro^{53} and Pro^{212} at the kinks of TM2 and TM7, and their neighboring hydrophobic residues, Leu^{52} and Ile^{55} (TM2) and Leu^{211} and Leu^{214} (TM7), form a flat hydrophobic patch at the center of the interface between the core domain and the gating bundle (Fig. 4, C and E), which probably enables the sliding motion of the gating bundle important for the transition between the inward- and outward-facing states (*10*). In Mol A of CAX_Af, the corresponding hydrophobic patch is formed by Leu^{76}, Pro^{77}, and Ala^{80} (TM2), and Ala^{253}, Pro^{257}, and Ile^{260} (TM7) (Fig. 4A). In contrast, in Mol B, the hydrophobic patch is split by the gap between Pro^{77} and Pro^{257} (Fig. 4B). Thus, the H^+ binding to CAX_Af closes the gap in the hydrophobic patch and enables the gating bundle to slide to the outward-facing state. Consistent with this mechanism, gating bundle in Mol A is slightly shifted toward the outward-facing state (Fig. 4D).

A structural comparison of the Ca^{2+} binding sites between CAX_Af and NCX_Mj suggested that Ca^{2+} binding induced conformational changes in TM2 and TM7. In the structure of NCX_Mj, the distance between the backbone carbonyls at the kinks of TM2 and TM7 (Thr^{50} and Thr^{209}) (Fig. 4, C and F) that coordinate Ca^{2+} is 4.1 Å (Fig. 4C). In contrast, in Mol B of CAX_Af, the distance between the corresponding carbonyl oxygen atoms is 5.6 Å (Fig. 4B). Consequently, TM2 and TM7 of CAX_Af are twisted toward the gating bundle, as compared with those of NCX_Mj (Fig. 4F and fig. S11). The twisting of TM7 is more significant than that of TM2 (fig. S11B). The structural comparison suggests that Ca^{2+} binding to CAX_Af induces the twisting of TM2 and TM7 toward the H^+/Ca^{2+} binding pocket (Fig. 4F). This twisting changes the directions of the backbone carbonyls at the kink of TM2 and TM7, and also the side chains of Glu^{78} and Glu^{258}, thereby enabling optimal coordination geometry for the Ca^{2+} as observed in NCX_Mj (Fig. 4F and fig. S11B). Thus, similar to the case of H^+ binding, Ca^{2+} binding brings Pro^{77} and Pro^{257} close together (Fig. 4F and fig. S11). Finally this closing the gap enables the sliding of the gating bundle.

In conclusion, the crystal structure of CAX_Af revealed the inward-open conformation of the CaCA protein, which revealed the alternate